HHS Public Access

Author manuscript

Mol Cell. Author manuscript; available in PMC 2023 October 20.

Published in final edited form as:

Mol Cell. 2022 October 20; 82(20): 3901–3918.e7. doi:10.1016/j.molcel.2022.09.007.

Histone methylation antagonism drives tumor immune evasion in squamous cell carcinomas

Yinglu Li[1,*], **Elizabeth M. Goldberg**[1,*], **Xiao Chen**[1,14,*], **Xinjing Xu**[1], **John T. McGuire**[1], **Giuseppe Leuzzi**[1], **Dimitris Karagiannis**[1], **Tiffany Tate**[2], **Nargess Farhangdoost**[3,4], **Cynthia Horth**[3,4], **Esther Dai**[1], **Zhiming Li**[5], **Zhiguo Zhang**[1,5,6,7], **Benjamin Izar**[7,8,9], **Jianwen Que**[10], **Alberto Ciccia**[1,7], **Jacek Majewski**[3,4], **Angela J. Yoon**[11], **Laurie Ailles**[12,13], **Cathy Lee Mendelsohn**[1,2,7], **Chao Lu**[1,7,15,#]

[1]Department of Genetics and Development, Columbia University Irving Medical Center, New York, NY 10032, USA

[2]Department of Urology, Columbia University Irving Medical Center, New York, NY 10032, USA

[3]Department of Human Genetics, McGill University, Montreal, QC H3A 1B1, Canada

[4]McGill University Genome Centre, Montreal, QC H3A 0G1, Canada

[5]Institute for Cancer Genetics, Columbia University Irving Medical Center, New York, NY 10032, USA

[6]Department of Pediatrics, Columbia University Irving Medical Center, New York, NY 10032, USA

[7]Herbert Irving Comprehensive Cancer Center, Columbia University Irving Medical Center, New York, NY 10032, USA

[8]Department of Medicine, Division of Hematology and Oncology, Columbia University Irving Medical Center, New York, NY 10032, USA

[9]Columbia Center for Translational Immunology, Columbia University Irving Medical Center, New York, NY 10032, USA

[10]Division of Digestive and Liver Diseases, Department of Medicine, Columbia Center for Human Development, Columbia University Irving Medical Center, New York, NY 10032, USA

[#]Corresponding Author: Chao Lu, PhD, cl3684@cumc.columbia.edu.

[*]These authors contributed equally

AUTHOR CONTRIBUTIONS

Y.L., E.M.G., X.C. and C.L. conceived the study. Y.L., E.M.G., X.C. executed the experimental work with the help of X.X., J.T.M., G.L., D.K., E.D. and T.T. N.F., C.H., Z.L., Z.Z., B.I., J.Q., A.C., J.M., A.J.Y. and L.A. provided reagents, expertise, and feedback. C.L.M. and C.L. supervised the study. Y.L., E.M.G., X.C. and C.L. wrote the manuscript, with contributions and input from all of the authors.

DECLARATION OF INTERESTS

B.I. is a paid consultant for Volastra Therapeutics. Other authors declare no competing interests.

SUPPLEMENTAL INFORMATION

Document S1. Figures S1–S7, Table S1 and S4

[11]Division of Oral and Maxillofacial Pathology, Columbia University College of Dental Medicine and Department of Pathology & Cell Biology, Columbia University Irving Medical Center, New York, NY 10032, USA

[12]Princess Margaret Cancer Centre, University Health Network, Toronto, ON M5G 1L7, Canada

[13]Department of Medical Biophysics, University of Toronto, Toronto, ON M5G 1L7, Canada

[14]Present address: Marine College, Shandong University, Weihai, 264209, China

[15]Lead Contact

SUMMARY

How cancer-associated chromatin abnormalities shape tumor-immune interaction remains incompletely understood. Recent studies have linked DNA hypomethylation and de-repression of retrotransposons to anti-tumor immunity through the induction of interferon response. Here, we report that inactivation of the histone H3K36 methyltransferase NSD1, which is frequently found in squamous cell carcinomas (SCC) and induces DNA hypomethylation, unexpectedly results in diminished tumor immune infiltration. In syngeneic and genetically engineered mouse models of head and neck SCC, NSD1-deficient tumors exhibit immune exclusion and reduced interferon response despite high retrotransposon expression. Mechanistically, NSD1 loss results in silencing of innate immunity genes, including the type III interferon receptor IFNLR1, through depletion of H3K36 di-methylation (H3K36me2) and gain of H3K27 tri-methylation (H3K27me3). Inhibition of EZH2 restores immune infiltration and impairs the growth of *Nsd1* mutant tumors. Thus, our work uncovers a druggable chromatin crosstalk that regulates the viral mimicry response and enables immune evasion of DNA hypomethylated tumors.

Graphical Abstract

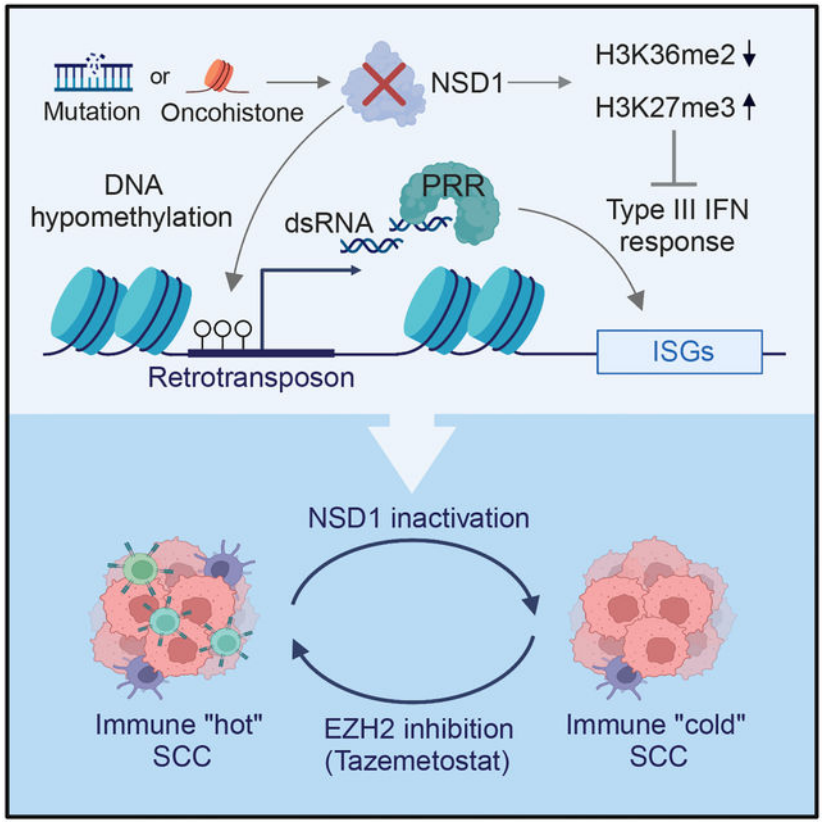

eTOC Blurb

Li et al. show that NSD1 inactivation in squamous cell carcinomas (SCCs) results in transcriptional silencing of innate immunity genes and diminished tumor immune infiltration through depletion of H3K36me2 and gain of H3K27me3. Inhibition of EZH2 reactivates interferon response, restores immune infiltration and impairs the growth of NSD1 mutant SCC.

INTRODUCTION

Tumor genome sequencing studies have uncovered that chromatin modifiers and modulators are frequently mutated in a wide array of human cancers (Shen and Laird, 2013). Furthermore, inhibitors of chromatin-modifying enzymes are approved to treat hematologic and soft tissue malignancies (Bates, 2020). While chromatin dysregulation has emerged as a molecular hallmark of cancer and an attractive target for therapeutic intervention, its contribution to tumor-immune interaction, particularly in the context of genomically complex adult epithelial cancers, remains poorly characterized.

Recurrent deletions and loss-of-function mutations affecting NSD1 - a histone methyltransferase that specifically catalyzes di-methylation of histone H3 Lys36 (H3K36me2) - are identified in 10–15% of head and neck squamous cell carcinomas (HNSCC) as well as in lung and cervical SCC (LUSC and CSCC) (Campbell et al., 2018; Cancer Genome Atlas, 2015; Papillon-Cavanagh et al., 2017). Neomorphic histone $H3^{K36M}$ mutations, which can biochemically inhibit the methyltransferase activity of NSD1, are also

found in HNSCC and LUSC and show mutual exclusivity with *NSD1* mutations (Papillon-Cavanagh et al., 2017). Together, *NSD1* and $H3^{K36M}$ mutations define a molecularly and clinically distinct subgroup of HNSCC characterized by global depletion of the histone mark H3K36me2. Demarcating early gene bodies and intergenic regions that are transcriptionally active, H3K36me2 antagonizes the gene-silencing activity of Polycomb Repressive Complex 2 (PRC2) and its product histone H3K27 tri-methylation (H3K27me3) (Marango et al., 2008; Streubel et al., 2018; Yuan et al., 2011). In addition, H3K36me2 promotes DNA methylation by guiding the recruitment of the *de novo* DNA methyltransferase DNMT3A (Shirane et al., 2020; Weinberg et al., 2019; Xu et al., 2020). Accordingly, HNSCC patient samples and cell lines harboring *NSD1* or $H3^{K36M}$ mutations exhibit genome-wide gain of H3K27me3 and loss of DNA methylation (Papillon-Cavanagh et al., 2017; Weinberg et al., 2019). However, the oncogenic mechanism and therapeutic implication of NSD1 inactivation-induced epigenome reprogramming in SCC remain unclear.

In somatic tissues, DNA methylation is critical for the silencing of endogenous retrotransposons and germline-specific genes (Jones, 2012). Accordingly, in several preclinical solid tumor models, low-dose treatment of DNA hypomethylating agent 5-azacytidine de-represses retrotransposons (Chiappinelli et al., 2015; Roulois et al., 2015). Aberrant transcription of these endogenous viral repetitive elements leads to the accumulation of double-stranded RNA (dsRNA), which can be sensed by cytoplasmic pattern recognition receptors (PRRs) such as MDA5/RIG-I involved in host virus defense. This “viral mimicry” response triggers type I interferon (IFN) production and initiates the activation of the Janus kinase (JAK) - signal transducer and activator of transcription (STAT) signaling pathway. The JAK-STAT signaling pathway is the principal mechanism to control the expression of IFN-stimulated genes (ISGs). ISG activation, in turn, facilitates tumor antigen presentation and anti-tumor adaptive immunity. Based on these findings, combined treatments of DNA hypomethylating agents and immune checkpoint inhibitors are actively being evaluated in clinical trials (Chiappinelli et al., 2016).

Unexpectedly, despite global DNA hypomethylation, transcriptomic analyses of *NSD1*/$H3^{K36M}$ mutant HNSCC patient samples and cell lines suggest that they are immune “cold” with significantly reduced presence of lymphocytes and expression of ISGs compared to wildtype counterparts (Brennan et al., 2017; Farhangdoost et al., 2021). Pan-cancer analysis of TCGA dataset also identified *NSD1* as one of the 12 cancer genes associated with immune evasion (Thorsson et al., 2018). These findings are further corroborated by a recent report showing that across all TCGA cancer types, there was a strong and positive correlation between levels of tumor DNA methylation and immune infiltration (Jung et al., 2019). Therefore, it appears that in contrast to acute pharmacological inhibition of DNA methylation, chronically hypomethylated cancer cells, such as those with NSD1 inactivation, have evolved to tolerate viral mimicry response and escape host immune surveillance through unknown mechanisms.

To explore this hypothesis, we developed two immunocompetent mouse models of HNSCC to test if NSD1 loss plays a role in suppressing tumor immunogenicity and immune infiltration. We demonstrated that in NSD1 mutant cells, depletion of H3K36me2 was followed by elevated H3K27me3 and transcriptional silencing of immune response genes

including those involved in type I/III IFN and JAK-STAT signaling pathways. Reactivation of interferon response through the inhibition of PRC2 and removal of H3K27me3 could effectively restore immune infiltration and impair the growth of NSD1-deficient tumors. These studies thus provide mechanistic and therapeutic insights into how histone methylation crosstalk can be hijacked by cancer cells to facilitate immune exclusion.

RESULTS

NSD1 loss reduces tumor immune infiltration in syngeneic HNSCC mouse model

TCGA pan-cancer analysis identified *NSD1* mutation as one of the 12 somatic variations linked to reduced tumor leukocyte fraction (Thorsson et al., 2018). Indeed, *NSD1* mutant HNSCC, LUSC, and CSCC patient samples exhibited significantly lower leukocyte fraction compared to *NSD1* wildtype samples (Figure S1A). We used another computational platform TIMER (Li et al., 2016) to estimate the levels of six tumor-infiltrating immune subsets based on bulk RNA-seq data and found their decreased presence in *NSD1* mutant HNSCC patient samples (Figure S1B). Analysis of a published HNSCC single-cell RNA-seq dataset (Puram et al., 2017) also demonstrated that *NSD1* mutant tumor had the highest purity with a minimal presence of various immune cell types (Figure S1C). Therefore, *NSD1* mutations in human SCC are tightly associated with reduced tumor immune infiltration.

To determine if NSD1 loss causes tumor immune evasion, we knocked out *Nsd1* using CRISPR-Cas9 in MOC1 cells (Figure S1D). MOC1 cells are established from carcinogen-induced oral SCC in C57BL/6 mice (Judd et al., 2012b). When transplanted into C57BL/6 mice, MOC1 cells form SCC tumors with moderate levels of immune infiltration (Judd et al., 2012a). Wildtype (WT) and two independent *Nsd1* knockout (*Nsd1* KO) clones of MOC1 cells were subcutaneously injected into C57BL/6 mice. Tumors of comparable size were harvested 35–38 days after transplantation and subjected to flow cytometry and immunofluorescence (IF) analysis of tumor immune microenvironment (Figure 1A, Figure S1E–F). Compared to *Nsd1* wildtype MOC1 tumors, *Nsd1* KO tumors had minimal levels of NSD1 protein expression and H3K36me2 (Figure 1B), and showed significantly reduced presence of T cells, CD8+ T cells and natural killer (NK) cells (Figure 1C). We also observed similar findings by IF staining, which revealed that in contrast to wildtype tumors, the depletion of NSD1 markedly abolished the invasion of CD8+ T cells and NK cells into Keratin5 (K5)-positive SCC compartment (Figure 1D, 1F). Interestingly, while flow cytometry analysis suggested that *Nsd1* KO tumors had increased amounts of intra-tumoral macrophages, IF staining showed that these macrophages were largely restricted to K5-negative stromal components (Figure 1C, 1E). Collectively, these results indicate that loss of NSD1 promotes exclusion of multiple immune cell types from the tumor microenvironment.

To examine the impact of immune exclusion on the growth of *Nsd1* KO tumors, we implanted *Nsd1* wildtype or KO MOC1 cells into either immunocompetent C57BL/6 mice or immunodeficient NOD.*Cg-Prkdc*^{scid} *Il2rg*^{tm1Wjl}/SzJ (NSG) mice. While wildtype MOC1 tumor growth was markedly more aggressive in NSG mice as expected, this trend was less pronounced for *Nsd1* KO tumors (Figure 1G–I), suggesting that *Nsd1* KO tumor growth is less sensitive to the presence of host immune surveillance.

Ablation of *Nsd1* induces immune-cold phenotype in a model of carcinogen-induced oral SCC

To assess the impact of NSD1 loss on tumor immune evasion in another setting that more precisely reflects the tissue-specific immune milieu, we generated *Nsd1* conditional knockout mice and subjected them to a model of chemically induced oral SCC. Mice carrying a floxed allele of *Nsd1* were crossed with $Krt5^{CreERT2}$ to generate $Nsd1^{f/f}$; $Krt5^{CreERT2}$ mice. $Krt5^{CreERT2}$ mice contain a transgene expressing tamoxifen-inducible Cre recombinase under the control of the bovine *Krt5* promoter (Indra et al., 1999). The *Krt5* promoter directs gene expression from E13.5 in the basal compartment of stratified oral epithelium, epidermis, and the outer root sheaths of hair follicles (Blanpain and Fuchs, 2006). This strategy thus enabled the conditional disruption of *Nsd1* in the basal cells of stratified epithelium in tamoxifen-gavaged 6–8 weeks old $Nsd1^{f/f}$; $Krt5^{CreERT2}$ animals (Figure 2A). Loss of NSD1 was verified at both mRNA and protein levels (Figure S2A–B). Notably, NSD1 depletion had minimal effects on the oral epithelium, as assessed by IF staining of proliferation marker Ki67, basal squamous marker p63, and lingual interpapillary marker keratin-13 (Figure S2B). These results suggest that NSD1 loss does not significantly impact oral epithelium homeostasis in adult mice.

We next subjected $Nsd1^{f/f}$; $Krt5^{CreERT2}$ mice to a well-established model of oral SCC carcinogenesis induced by 4-nitroquinoline (4NQO)-infused drinking water. 4NQO is a DNA adduct-forming agent that acts as a surrogate for tobacco exposure, a major risk factor for HPV-negative HNSCC and LUSC. The 4NQO-induced model has been demonstrated to faithfully recapitulate the histology and molecular signatures of human HNSCC (Nauta et al., 1995; Wang et al., 2019). $Nsd1^{f/f}$; $Krt5^{CreERT2+}$ or $Nsd1^{f/f}$; $Krt5^{CreERT2-}$ mice (*Nsd1* KO or *Nsd1* WT, respectively) received tamoxifen for five days, followed by drinking water containing 4NQO for 16 weeks prior to returning to normal drinking water for an additional 10 weeks (Figure 2A). Consistent with previous reports, by week 26, all mice developed grossly visible lesions of the tongue. Absence of NSD1 expression was observed in lesions from *Nsd1* KO but not *Nsd1* WT mice (Figure S2C). Importantly, IF staining revealed significantly reduced infiltration of CD8+ T cells, macrophages and natural killer (NK) cells into Krt5+ tumor epithelial compartment in *Nsd1* KO lesions compared to *Nsd1* WT lesions (Figure 2B–D), consistent with findings from the MOC1 syngeneic HNSCC mouse model.

NSD1 mutant HNSCC patient samples show immune exclusion

We sought to test if the spatial patterns of tumor-infiltrating lymphocytes observed in our immunocompetent mouse models can be observed in patient samples. We assembled a cohort of treatment-naïve, primary HPV-negative HNSCC tumors where the mutational status of 112 HNSCC-associated genes including *NSD1* has been determined. Nine samples with *NSD1* inactivating mutations or deletions and ten *NSD1* wildtype (WT) samples with matching patient demographics and tumor grade/stage were included in the analysis (Table S1). Sections from formalin-fixed, paraffin-embedded (FFPE) tumor tissue blocks were IF stained to confirm the loss of NSD1 expression and H3K36me2 (Figure S2D). *NSD1* mutant tumor samples demonstrated a significantly decreased presence of tumor-infiltrating CD8+ T cells and NK cells across all TNM stages (Figure 2E–F, Figure S2E–F). These results

agree with conclusions inferred from tumor transcriptomes (Figure S1B–C) and indicate that NSD1 loss likely drives an immune exclusion phenotype in mouse and human HNSCC.

NSD1 loss decreases the expression of interferon-stimulated genes

To investigate how loss of NSD1 shapes the tumor-immune microenvironment, we deleted *NSD1* using CRISPR-Cas9 in an *NSD1* wildtype human HNSCC cell line Cal27 and performed RNA-seq. Genes involved in axon guidance were up-regulated in *NSD1* KO Cal27 cells (Figure S3A). Notably, interferon response and signaling pathways - critical regulators of tumor immunogenicity - emerged among the top enriched gene ontology (GO) groups of genes significantly downregulated (Fold change >2; FDR < 0.1) in *NSD1* KO cells (Figure 3A). Consistently, gene set enrichment analysis (GSEA) revealed that downregulated genes upon *NSD1* deletion were significantly enriched for interferon-stimulated genes (ISGs) (Figure 3B) (Liu et al., 2019). Decreased expression of ISGs was also observed when comparing *NSD1* mutant to wildtype HNSCC cell lines (Figure 3B–C, Figure S3B), or *NSD1* mutant to wildtype TCGA HNSCC patient samples (Figure S3C). We further performed qRT-PCR of representative ISGs, which showed that loss of NSD1 in Cal27, as well as two additional *NSD1* wildtype HNSCC lines (FaDu and Detroit 562) resulted in reduced ISG expression (Figure 3D–F). Lipopolysaccharide (LPS) and herring testes DNA (htDNA) are pathogen-associated molecular patterns (PAMPs) commonly used to mimic bacteria or viral infection to activate interferon response and the transcription of ISGs (Kawai and Akira, 2010; Mackenzie et al., 2017). Cal27 *NSD1* KO cells were unable to induce the expression of ISGs upon treatment with LPS or htDNA (Figure 3G–H). Importantly, tumor expression of ISGs such as IRF7, MX1 and RSAD2 were diminished upon *Nsd1* deletion in both syngeneic (Figure S3D) and carcinogen-induced (Figure 3I) mouse models of HNSCC. *NSD1* mutant HNSCC patient samples also displayed decreased IRF7 and MX1 expression (Figure 3J). Therefore, NSD1 loss appears to impair both basal and PAMP-induced ISG expression *in vitro* and *in vivo*.

Beyond HNSCC, *NSD1* is recurrently mutated and deleted in SCCs of other body sites such as LUSC (Papillon-Cavanagh et al., 2017). We found that similar to HNSCC, the copy number of *NSD1* is significantly positively correlated with ISG expression in TCGA LUSC patient samples (Figure S3E–F). Deletion of *NSD1* in a human LUSC line SK-MES-1 also led to decreased expression of ISGs (Figure S3G–H), suggesting that the function of NSD1 in regulating ISG expression is likely conserved across SCC of different body sites.

NSD1 loss impairs interferon signaling response

In cancer cells, both chromosomal instability and de-repression of endogenous retroviral elements could induce an interferon response and expression of ISGs (Figure 4A) (Chiappinelli et al., 2015; Mackenzie et al., 2017; Roulois et al., 2015). We found that *NSD1* KO Cal27 cells or *NSD1* mutant BICR78 and SKN-3 cells showed elevated levels of retrotransposons including LINE-1/L1 and SINE/Alu (Figure S4A), consistent with their genome-wide decrease in DNA methylation. Moreover, *NSD1* deletion resulted in aberrant accumulation of retrotransposon-derived double-stranded RNA (dsRNA) in Cal27 cells (Figure 4B). We also examined public tumor whole-genome sequencing datasets (Rodriguez-Martin et al., 2020) and found that the levels of L1-mediated retrotransposition,

structural variation and mutational burden were elevated in *NSD1* mutant HNSCC patient samples (Figure S4B). Consistently, the frequency of micronuclei was significantly higher in *NSD1* mutant relative to wildtype HNSCC cell lines (Figure S4C). Taken together, these results suggest that *NSD1* mutant cancer cells show an increase in genomic and epigenomic instability yet reduced ISG expression. We therefore reason that PAMP sensing and interferon signaling pathways could be impaired upon NSD1 loss.

Genome instability and micronuclei are known to activate the cytosolic DNA sensor cGAS and its adaptor STING (Mackenzie et al., 2017). We first assessed and found modest and variable reductions in the levels of cGAS/STING and their downstream effectors 2'3'-cGAMP, TBK1 and IRF3 in *NSD1* KO cells (Figure S4D–E). The expression of LPS receptor TLR4 was also comparable between wildtype and *NSD1* KO cells (Figure S4E).

Retrotransposon-derived dsRNA can be sensed by cytosolic pattern recognition receptors (PRRs) such as MDA5/MAVS/RIG-I, which activate the expression of Type I/III interferons through IRF7 (Kawai and Akira, 2010; Sadler and Williams, 2008; Ye et al., 2019). Type I/III interferons can, in turn, bind to interferon receptors, initiate JAK/STAT signaling cascade and induce the expression of ISGs (Figure 4A). We observed that the protein levels of MDA5, IRF7, and total and phosphorylated STAT1 were reduced in *NSD1* KO Cal27 and *NSD1* mutant BICR-78 and SKN-3 cells (Figure 4C–D). Similar decreases in phospho-STAT1 and IRF7 were observed following the knockout of *NSD1* in SK-MES-1 cells, suggesting that NSD1 also regulates interferon response in LUSC cells (Figure S4F). Full-length NSD1 is difficult to be ectopically expressed as it contains ~2700 amino acids (Figure S4G). We managed to express a truncated NSD1 harboring the catalytic SET domain (Figure S4G–H) in Cal27 *NSD1* KO cells. Introducing truncated NSD1 was able to restore levels of H3K36me2, STAT1, STAT1 phosphorylation and downstream ISGs expression (Figure 4E–F). Intriguingly, reconstitution of an enzymatically dead mutant (R2017Q) NSD1 failed to rescue interferon signaling and ISG expression in Cal27 *NSD1* KO cells (Figure 4E–F), indicating the importance of NSD1's methyltransferase activity in regulating tumor interferon response. To further test the causal relationship between NSD1 and the interferon signaling pathway, we corrected the *NSD1* insertion/frameshift mutation at c.5616 in SKN-3 cells using CRISPR-Cas9 prime editing (Anzalone et al., 2019). Upon correction and restoration of NSD1 expression and H3K36me2, STAT1 phosphorylation was markedly increased (Figure S4I).

To determine the functional role of interferon signaling pathway in mediating NSD1's impact on ISG expression, we performed gain- and loss-of-function studies of STAT1, a key component of the Type I/III interferon response. We ablated *STAT1* in parental Cal27 cells using CRISPR-Cas9 (Figure S4J). *STAT1* knockout largely phenocopied the effect of NSD1 loss on reducing IRF7 and IRF9 protein expression (Figure S4J) and silencing of ISGs (Figure S4K). Conversely, we employed CRISPR activation (CRISPRa) system (Chavez et al., 2015) to augment STAT1 expression and phosphorylation in *NSD1* KO Cal27 cells to levels that are comparable to wildtype Cal27 cells (Figure 4G). Expression of ISGs and IRF7 was significantly rescued in NSD1-deficient cells following the reactivation of STAT1 (Figure 4H).

Increased H3K27 methylation in NSD1-deficient HNSCC cells represses the transcription of Type III interferon receptor IFNLR1

To investigate the epigenetic mechanism by which NSD1 loss suppresses the interferon signaling pathway, we assessed the genome-wide distribution of H3K36me2 using CUT&Tag in *NSD1* wildtype or KO Cal27 cells. Since H3K36me2 has been implicated in antagonizing the activity of PRC2 and the deposition of its product H3K27 methylation (Marango et al., 2008; Streubel et al., 2018; Yuan et al., 2011), we also performed CUT&Tag for H3K27me3, a histone mark with an established role in transcriptional silencing. As expected, we observed a genome-wide depletion of H3K36me2 and gain of H3K27me3 in *NSD1* KO cells (Figure 5A), and the changes in H3K36me2 and H3K27me3 were significantly anti-correlated (Figure S5A). Transcriptionally downregulated genes were associated with decreased H3K36me2 in *NSD1* KO cells. These genes had modest levels of H3K27me3 enrichment at promoters, which were further augmented by loss of NSD1 (Figure S5B–C). In contrast, transcriptionally upregulated genes were not associated with changes in H3K27me3 or H3K36me2, suggesting that they likely represent secondary response genes (Figure S5B–C, Table S2).

GO analysis of genes that gained H3K27me3 upon *NSD1* KO revealed that the top enriched functional groups included genes involved in immune response and STAT activation (Figure 5B) such as *IFNA* family genes, *IL19* and *IFNLR1*. We focused on *IFNLR1*, which encodes for the receptor of Type III interferon lambda (IFN-λ) (Kotenko et al., 2003; Sheppard et al., 2003), for further functional analysis. NSD1 loss led to the replacement of H3K36me2 with H3K27me3 at the promoter region of *IFNLR1* and its decreased transcription (Figure 5C). We performed flow cytometry and found that cell surface expression of IFNLR1 was significantly reduced in *NSD1* KO Cal27 cells (Figure 5D). Consistently, analysis of public ATAC-seq datasets of TCGA HNSCC patient samples (Corces et al., 2018) revealed that *NSD1* mutant tumors displayed diminished chromatin accessibility at *IFNLR1* promoter compared to *NSD1* wildtype tumors (Figure S5D). These findings were further demonstrated in carcinogen-induced oral SCC mouse model: compared to *Nsd1* wildtype tumors which expressed IFNLR1 in Krt5+ tumor epithelial compartment, *Nsd1*-deleted tumors had markedly decreased IFNLR1 expression (Figure 5E). In both Cal27 and MOC1 cells, ablation of *NSD1* did not significantly alter the production of IFN-λ (Figure S5E–F) but suppressed the stimulatory effects of IFN-λ on STAT1 phosphorylation and ISG expression (Figure S5G–I). Knockdown of IFNLR1 in Cal27 cells using two independent siRNAs reduced STAT1 phosphorylation and expression of ISGs, recapitulating the impact of NSD1 loss (Figure 5F–G). Furthermore, we generated CRISPR-Cas9-mediated *Ifnlr1* KO MOC1 cells (Figure 5H) and subcutaneously injected those into C57BL/6 mice. IF staining of immune cells demonstrated that ablation of *Ifnlr1* decreased CD8+ T cell and macrophage infiltration into tumor epithelium (Figure 5I, Figure S5J). Collectively, these results suggest that H3K27me3-associated epigenetic silencing of *IFNLR1* contributes to the impaired Type III interferon response and immune infiltration of NSD1-deficient HNSCC tumors.

Pharmacologic inhibition of EZH2 but not DNMT1 restores interferon response in NSD1-deficient cells

We next tested if depletion of H3K27me3 through pharmacologic inhibition of PRC2 could rescue the impaired interferon response in NSD1-deficient cells. We applied an FDA-approved inhibitor of EZH2, EPZ-6438/Tazemetostat, to *NSD1* KO Cal27 cells and performed RNA-seq and CUT&Tag for H3K27me3 and H3K36me2. Approximately two-thirds (444/695) of differentially expressed genes between wildtype and *NSD1* KO Cal27 cells were restored by EPZ-6438 (Figure S6A). Genes upregulated upon EPZ-6438 treatment were predominantly linked to interferon signaling pathways (Figure 6A). Consistently, we observed that EPZ-6438 treatment effectively restored the expression of ISGs and IRF7/9, MDA5, STAT1 and phosphorylated STAT1 in *NSD1* KO Cal27 and FaDu cells (Figure 6C–D, Figure S6B). These global changes are also evident at the *IFNLR1* locus, where we observed a depletion of H3K27me3, a modest increase in H3K36me2 and rescued transcription (Figure 5C, Figure S6C). Cell surface expression of IFNLR1 was significantly restored following EZH2 inhibition (Figure S6D). Depletion of IFNLR1 abolished the rescue effects of EPZ-6438 on ISG expression in *NSD1* KO cells (Figure 6E), suggesting that the impact of EZH2 inhibition on interferon response is, at least in part, mediated through Type III interferon signaling. Finally, treatment of EPZ-6438 (200 mg/kg) enhanced the expression of IRF7 in *Nsd1* KO MOC1 tumors (Figure 6F). Interestingly, inhibition of EZH2 also led to increased ISG expression and interferon signaling in wildtype Cal27 cells (Figure 6B–C), likely due to the modest enrichment of H3K27me3 at these genes (Figure S5B) which may partially suppress their transcription. However, these *in vitro* findings did not extend to *in vivo* setting, as EPZ-6438 treatment failed to further increase IRF7 expression in *Nsd1* wildtype MOC1 tumors (Figure 6F).

As an important control, we measured and found that EPZ-6438 treatment did not increase the amount of dsRNA (Figure S6E). Therefore, the effect of EZH2 inhibition on restoring interferon response in NSD1-deficient cells could not be attributed to further de-repression of retrotransposons. This is in sharp contrast to the treatment of DNA hypomethylating agents (5-azacytidine and SGI-110), which globally increased dsRNA accumulation and augmented interferon response and ISG expression in *NSD1* wildtype cells yet had minimal impact on these pathways in NSD1-deficient cells (Figure S6E–G). These results lend further support to the notion that the impaired tumor immunogenicity by NSD1 loss is linked to the sensing and downstream innate immune response, rather than the production, of retrotransposon-derived dsRNA.

EZH2 inhibitor elicits immune infiltration and inhibits the growth of NSD1-deficient SCC tumors

To examine whether the reestablishment of interferon response by EZH2 inhibition translates into restored anti-tumor immunity *in vivo*, we implanted parental and *Nsd1* KO MOC1 cells subcutaneously into immunocompetent C57BL/6 mice. Mice were orally administered with vehicle control or 200mg/kg or 400mg/kg of EPZ-6438 when tumor size reached to approximate 100 mm^3, which depleted global H3K27me3 *in vivo* (Figure S7A). At both doses, we observed that EPZ-6438 treatments effectively halted the growth of *Nsd1* KO but not parental MOC1 tumors and improved the survival of tumor-bearing mice

accordingly (Figure 7A–B, Figure S7B). To determine if this growth inhibitory effect of EPZ-6438 depends on a functional host immune system, we repeated the tumor implantation study in immunodeficient (*Foxn1*^{nu}) mice. EPZ-6438 had minimal effect on limiting the growth of *Nsd1* KO MOC1 tumors in *Foxn1*^{nu} mice, suggesting that its anti-tumor effects are likely unrelated to inhibiting cancer cell-intrinsic proliferation (Figure 7C, Figure S7B). We therefore assessed the landscape of tumor-infiltrating immune cells before and after the treatment of EPZ-6438 by IF. This analysis revealed a significant increase in the number of intra-tumoral CD8+ T cells, CD11b+ macrophages and NK1.1+ NK cells in NSD1-deficient MOC1 tumors after EZH2 inhibition (Figure 7D–F). Consistent with the lack of elevated interferon response and growth inhibition by EPZ-6438 in wildtype MOC1 tumors (Figure 6F, Figure 7A), our IF analysis found comparable presence of leukocytes including CD8+ T cells, NK cells and macrophages in MOC1 wildtype tumors with or without EPZ-6438 treatment (Figure S7C–E). Thus, H3K27me3 depletion could not further enhance the migration of immune cells into wildtype MOC1 tumors. These results indicate that EPZ-6438 selectively blocks the growth of *Nsd1* KO tumors likely through augmenting tumor immunogenicity and immune infiltration.

DISCUSSION

Adult epithelial cancers, such as SCC, display relatively high mutation burden and chromosomal instability, leading to the release of single-stranded DNA (ssDNA) from the nucleus. Many of these tumors also experience replication-coupled progressive loss of DNA methylation (Zhou et al., 2018), which de-represses dsRNA-encoding retrotransposon elements. The accumulation of ssDNA and dsRNA in cancer cells can elicit a “pathogen-induced-like” innate immune response and the subsequent adaptive immunity (Jones et al., 2019). Therefore, the tumor-intrinsic innate immune response represents a key barrier to the development of genetically and epigenetically unstable cancers. Accordingly, recurrent mutations affecting genes involved in the antigen presentation pathway (*B2M* and *HLA*) and interferon signaling pathway (*IFNGR1*, *JAK1*, *JAK2*) have been associated with various cancer types (Gao et al., 2016; Shin et al., 2017; Zaretsky et al., 2016). In this study, we used both a syngeneic tumor implantation model and a genetic-engineered, carcinogen-induced model to demonstrate that *Nsd1* ablation results in an immune “cold” phenotype in SCC through epigenetic silencing of the tumor interferon response. The spatial distribution of immune cells in NSD1-deficient tumors is suggestive of immune exclusion, in which lymphocytes are restricted to the stroma at tumor borders, but fail to penetrate the tumor compartment. These results are mirrored in primary HNSCC patient samples: despite high mutation burden and DNA hypomethylation, *NSD1* mutant HNSCC are associated with a lack of immune infiltration. Notably, mutations in other epigenetic regulators, such as EZH2, G9a and mSWI/SNF complexes (ARID1A and PBRM1) (Burr et al., 2019; Ennishi et al., 2019; Kato et al., 2020; Li et al., 2020; Liu et al., 2020; Shen et al., 2018), have been implicated in shaping the tumor immune phenotype. Therefore, our findings support the notion that in addition to genetic alterations, cancer cells frequently exploit chromatin-based mechanisms to epigenetically suppress innate immune response and tumor immunogenicity.

We observed similar tumor growth rate between MOC1 *Nsd1* KO versus control cells, which seems inconsistent with the notion that immune evasion leads to enhanced tumor growth.

However, it is notable that *Nsd1* KO tumors grow much more slowly in immunodeficient (NSG) mice. Therefore, it appears that NSD1 loss facilitates tumor immune escape while limiting the rate of cancer cell proliferation. Interestingly, in addition to *NSD1*, mutations in *IDH1* are also correlated with tumor immune evasion in TCGA pan-cancer analysis (Thorsson et al., 2018). Mutant IDH1 impairs histone and DNA demethylation via production of the oncometabolite 2-hydroxyglutarate (Lu et al., 2012) and, similar to NSD1, inhibits the proliferation of cancer cells (Qing et al., 2021), representing another tradeoff between tumor intrinsic growth and immune evasion. We speculate that mutations in growth signaling pathways, such as *PI3KCA* activating mutations that are commonly found in HNSCC, may compensate for the negative impact of NSD1 loss on cancer cell fitness.

Our mechanistic investigation suggests that the perturbed antagonism between H3K36 and H3K27 methylation upon NSD1 loss results in a gain of H3K27me3 at genes involved in immune response and JAK-STAT signaling, including *IFNLR1* that encodes the receptor for Type III IFNs (IFN-λ). Knockdown of IFNLR1 was sufficient to phenocopy *NSD1* deletion's effect on silencing ISG expression *in vitro* and reducing tumor immune infiltration *in vivo*. Therefore, while we cannot exclude the contribution from other interferon response pathways, Type III IFNs appear to be an important mediator in the regulation of tumor immunity by NSD1. Type III and Type I IFNs share similar downstream signaling cascades in promoting antiviral or anti-tumor immunity with several distinctions. For example, IFN-λ response regulates a narrower set of ISGs and induces moderately expressed and long-lasting ISG expression, while Type I interferon stimulates highly expressed and short-lived ISGs (Marcello et al., 2006). Furthermore, while Type I IFNs are active in most tissues, the IFN-λ response and the expression of IFNLR1 are primarily restricted to mucosal epithelium (Ye et al., 2019), thus protecting barrier tissues from pathogen attacks. These findings may explain why mutations in *NSD1* are frequently found in SCCs of the aerodigestive tract but not other cancer types (Campbell et al., 2018). It remains unclear why innate immunity genes are preferentially affected by the imbalance between H3K36me2 and H3K27me3 in SCC cells. Our motif analysis found that gene promoters that gained H3K27me3 in *NSD1* KO cells were enriched for binding sites of interferon regulatory transcription factors such as IRF8 and MYB (Table S3). Therefore, we speculate that in epithelium tissues, NSD1 is recruited by interferon regulatory transcription factors to prevent PRC2-mediated silencing and maintain accessibility of interferon response genes.

Epigenetic inhibitors such as DNA hypomethylating agents have shown promise in boosting anti-tumor immunity by de-repressing repetitive elements and eliciting interferon responses (Chiappinelli et al., 2015; Roulois et al., 2015). Our results, however, suggest that in NSD1-deficient cancer cells, which already exhibit DNA hypomethylation and retrotransposon activation, further induction of dsRNA accumulation by DNMT inhibitors had minimal effect on interferon signaling. These results are consistent with a TCGA pan-cancer analysis showing that DNA hypomethylated patient tumor samples, counterintuitively, are also immune cold (Jung et al., 2019). We speculate that chronically hypomethylated and retrotransposon-high tumors have evolved mechanisms to impair innate and/or adaptive immunity during development, and thus are less responsive to therapeutic strategies that further increase levels of dsRNA and neoantigens. Instead, our data suggest that these

tumors may be highly vulnerable to the re-establishment of antigen sensing and signaling pathways, as demonstrated by the potent and specific effects of EZH2 inhibition on augmenting immune infiltration and impairing the growth of NSD1-deficient tumors. Notably, recent studies have reported a diverse array of context-specific effects of EZH2 inhibition on anti-tumor immunity, including de-repressing the MHC class I antigen presentation pathway (Burr et al., 2019; Ennishi et al., 2019; Zhou et al., 2020), activating the cGAS-STING pathway (Morel et al., 2021), and regulating effector T-cell function (Goswami et al., 2018; Gray et al., 2017; He et al., 2017). Taken together, these findings suggest that instead of a “one-size-fits-all” approach, maximizing the success of “viral mimicry”-inducing epigenetic therapy likely requires rational design of therapeutic strategies and patient stratification based on the specific genetic, chromatin and immunoediting landscape of individual tumors.

SCCs collectively represent the most frequent human solid tumors. HNSCC alone affects >63,000 new cancer cases per year in the US and causes significant morbidity and mortality (Johnson et al., 2020). Recently, anti-PD-1/PD-L1 immune checkpoint inhibitors have shown remarkable efficacy in treating HNSCC (Ferris et al., 2016). However, only a minority of patients respond to immune checkpoint inhibitors. Our study establishes a role for NSD1 loss in tumor immune evasion and offers strong incentives for clinical studies to assess the utility of NSD1 and H3K36me2 as biomarkers to predict response to immune checkpoint inhibitors for HNSCC and other SCC patients. Furthermore, the preclinical therapeutic benefit of FDA-approved EZH2 inhibitor Tazemetostat on restoring immune infiltration and inhibiting tumor growth warrants clinical assessment of Tazemetostat, alone or combined with immune checkpoint inhibitors, for treating NSD1-deficient SCC tumors. We believe that chromatin crosstalk such as H3K36-H3K27 methylation antagonism represents common and important mechanisms of tumor-immune interaction and opportunities for therapeutic intervention.

Limitations of the Study

Although we have demonstrated a functional role of NSD1 in shaping the tumor immune microenvironment in two independent mouse models of HNSCC, the relevance of these findings to human setting requires additional investigation. In HNSCC patient samples, *NSD1* mutation is tightly associated with immune exclusion. However, patient-derived or cell line-derived HNSCC xenograft studies in mice engrafted with humanized immune system are needed to establish causality. While the majority of transcriptional changes upon *NSD1* knockout can be rescued by EZH2 inhibition, the mechanism and functional significance of differentially expressed genes between wildtype and *NSD1* KO cells that are independent of H3K27me3 remain unclear. Furthermore, while histone is considered as the main substrate for NSD1, non-histone substrates of NSD1 have been described including NFkB/p65 (Lu et al., 2010). Therefore, our work does not exclude the possibility that methylation of non-histone proteins may also facilitate NSD1’s regulation of tumor interferon response and immune evasion. Lastly, while our results suggest that knockout of Type III interferon receptor IFNLR1 is sufficient to phenocopy NSD1 loss and reduce tumor immune infiltration, future functional studies are required to determine the contribution

from other similarly epigenetically silenced interferon response genes to the immune cold phenotype of *NSD1* mutant cancers.

STAR METHODS

RESOURCE AVAILABILITY

Lead Contact—Further information and requests for resources and reagents should be directed to and will be fulfilled by the lead contact Chao Lu (cl3684@cumc.columbia.edu).

Materials Availability—All the materials generated in this study are accessible upon request.

Data and Code Availability

- RNA-seq and CUT &Tag data reported in this paper have been deposited at GEO and are publicly available as of the date of publication. Accession numbers can be found at GSE186239. This paper also analyzes existing, publicly available ATAC-seq data from The Cancer Genome Atlas (TCGA). The data can be assessed from The Genomic Data Common (GDC), https://gdc.cancer.gov/about-data/publications/ATACseq-AWG.
- This paper does not report original code.
- Any additional information required to reanalyze the data reported in this paper is available from Chao Lu upon request (cl3684@cumc.columbia.edu).

Experimental model and subject details

Cell lines and Cell Culture: Cal27 (ATCC), FaDu (ATCC), Detroit 562 (ATCC), PE/CA-PJ15 (Sigma-Aldrich), SKN-3 (JCRB cell bank), BICR78 (Sigma-Aldrich) and SK-MES-1(ATCC) cells were cultured in DMEM (Sigma-Aldrich) with 10% FBS (Sigma-Aldrich). MOC1 (Kerafast) was cultured in IMDM (Cytiva) and Hams Nutrient Mixture F10-F12 (Cytiva) at 2:1 ratio with 5% FBS, 5 ug/mL Insulin (Sigma-Aldrich), 40 ng/mL Hydrocortisone (Sigma-Aldrich) and 5 ng/mL EGF (Sigma-Aldrich). All cells were supplied with 1x Penicillin-Streptomycin (Sigma-Aldrich) and kept at 37 degree in 5% CO_2 atmosphere. All cell lines were routinely tested for mycoplasma contamination.

***Nsd1* conditional knockout mice and carcinogen-induced oral SCC model:** $Nsd1^{f/f}$ mice were generated by electroporation of a targeting vector into HF4 (129/SvEv × C57BL/6) (FLP Hybrid) embryonic stem (ES) cells that introduces two loxP sites flanking *Nsd1* exon 3. After selection with G418 antibiotic, surviving clones were expanded for PCR analysis to identify recombinant ES clones. The Neo cassette in targeting vector was removed during ES clone expansion. Correctly targeted ES cell clone, validated by PCR, sequencing and southern blot analysis, was microinjected into C57BL/6 blastocysts. Resulting chimeras with a high percentage agouti coat color were mated to C57BL/6 wildtype mice to obtain germline transmission. $Krt5^{CreERT2}$ mice were obtained from D. Metzger and P. Chambon. All work with mice was approved by and performed under the regulations of the Columbia University Institutional Animal Care and Use Committee. Adult $Nsd1^{f/f}$; $Krt5^{CreERT2}$ mice

received oral gavage with tamoxifen (Sigma-Aldrich) dissolved in corn oil at a dose of 200 mg/kg. Mice received a total of three doses with tamoxifen over a period of 7 days. To induce development of oral tumors, eight-week old female and male *Nsd1*$^{f/f}$; *Krt5*$^{CreERT2+/-}$ mice that received tamoxifen were treated with 50 μg/ml of 4NQO (Sigma-Aldrich) in drinking water for 16 weeks. Water was changed weekly. After 16 weeks, 4NQO use was stopped and mice received normal drinking water for an additional 10 weeks.

Xenograft experiments: 6–8 weeks-old male C57BL/6 mice, *Foxn1*^{nu} mice and NOD.Cg-PrkdcscidIl2rgtm1Wjl/SzJ (NSG) mice were purchased from The Jackson Laboratory. All mice were housed under specific-pathogen-free (SPF) condition and followed the guideline of Columbia University animal facility. All mice experiments were carried out with the protocol approved by the Institutional Animal Care and Use Committee (IACUC) at Columbia University. C57BL/6 mice or NSG mice were subcutaneously injected with MOC1 or MOC1 *Nsd1* KO cells (2×10^6 per injection) into the flank. Tumor growth was measured twice a week. Mice were sacrificed when tumor size reached to 1500 mm^3.

For EPZ-6438 treatment, C57BL/6 mice or *Foxn1*^{nu} mice were subcutaneously injected with MOC1 or MOC1 *Nsd1* KO cells (2×10^6 per injection) into the flank. Tumor growth was measured twice a week. EPZ-6438 was dissolved in sterile water with 0.5% NaCMC and 0.1% Tween 80. Vehicle only or EPZ-6438 (200 mg/kg or 400 mg/kg) were applied to mice via oral administration once a day when tumor size reaches to ~100 mm^3. Tumors were harvested for flow cytometry and IF staining 35–38 days after the implantation.

Method Details

Plasmid construction and Lentivirus production: Truncated-NSD1 (exon-10–21) cDNA was cloned into pCDH-EF1-MCS-IRES-Puro (System Biosciences). Site-specific mutation of truncated-NSD1 (R2017Q) was generated using a site-directed mutagenesis kit (Vazyme).

Lentivirus were generated by transfecting 293T cells with the indicated expression plasmids and the psPAX2 (Addgene) and pVSVG (Addgene) packaging vectors at a ratio of 4:2:3, respectively. Viral supernatants were collected 72 hrs after transfection and concentrated using the PEG Virus Precipitation Kit (SystemBio) according to the manufacturer's protocol.

CRISPR-Cas9 mediated gene knockout, prime editing and gene activation: To generate NSD1 KO cell lines from Cal27, SK-MES-1 and MOC1, sgRNAs (Table S4) against *NSD1* or *Nsd1* were cloned into pSpCas9(BB)-2A-GFP plasmid (Addgene) and transfected into target cells using Lipo-LTX (ThermoFisher). GFP-positive cells were sorted into single cells using Influx Cell Sorter 36hrs after transfection. Individual clones were validated by both immunoblotting and Amplicon-sequencing (Genewiz). FaDu *NSD1* KO and Detroit 562 *NSD1* KO cell lines have been previously described (Farhangdoost et al., 2021).

For CRISPR prime editing, pegRNA to correct *NSD1* mutation (c.5616dup) in SKN-3 cells and PE3 site were designed using Benchling (Table S4). Plasmid pU6-pegRNA-GG-acceptor (Addgene) was digested with BsaI-HF-v2. Oligos for PE2_sgRNA, scaffold, 3prime_extention and PE3 sgRNA were annealed and phosphorylated with T4 PNK. Golden

Gate Assembly of the annealed PE2_sgRNA, phos_scaffold, and 3prime_extention was performed with the previously digested acceptor plasmid. PE3 sgRNA oligos were similarly annealed, phosphorylated and ligated into pUiSEPR (gift from Scott Lowe lab). SKN-3 cells were transfected with prime editor expression plasmid (Addgene), pegRNA expression plasmid and nicking sgRNA at the ratio previously described (Anzalone et al., 2019) with Lipofectamine LTX. After 72 hours, cells were sorted for RFP. Successful prime editing was validated by both immunoblotting and Sanger sequencing.

For CRISPR activation of *STAT1*, cells were infected with dCas9VPR-Neo (gift from Scott Lowe lab) and selected with G418 (ThermoFisher) 48hrs after infection. Seven individual sgRNAs (Table S4) targeting *STAT1* promoter were cloned into pUiSEPR. Cells were infected with gRNA pool and selected with puromycin.

Immunohistochemistry (IHC) and immunofluorescence (IF) staining: For IF staining of dsRNA, cells seeded on glass coverslips were fixed with 4% paraformaldehyde and permeabilized with 0.2% Triton X-100 for 5 min. After PBS wash, samples were incubated with J2 antibody (SCICONS) overnight at 4°C. Samples were washed three times with PBS before incubating with Alexa Fluor 488 Goat anti-mouse secondary antibody (ThermoFisher) for 30 min. Samples were then counterstained with 4′,6-diamidino-2-phenylindole (DAPI) (ThermoFisher) solution in PBS for 20 min and washed three times with PBS. The coverslips were inverted onto gel mount on microscope slides, viewed and photographed with Zeiss Axiovert 200M microscope.

For tissue IHC and IF staining, mouse tongues/tumors were fixed overnight in 4% paraformaldehyde and embedded in paraffin. Serial sections of 5 μm were generated. For IHC of both mouse tissue and human HNSCC samples, paraffin sections were deparaffinized using HistoClear and rehydrated through a series of ethanol washes. Antigen retrieval was performed by boiling slides for 15 min in pH 9 buffer or 30 min in pH 6 buffer. Primary antibodies in 1% horse serum were incubated overnight at 4 °C. The next day, slides were washed with PBST twice for 10 min each and secondary antibodies were applied for 2 hr at room temperature. DAPI (4’6-diamidino-2-phenylindole) was applied as part of the secondary antibody cocktail for nuclear staining. Slides were sealed and with coverslips using DAKO mounting gel. Fluorescent images were collected using a Zeiss Axiovert 200M microscope with an apotome (Zeiss). Confocal microscopy was performed on a Nikon A1R MP confocal microscope (Nikon Instruments). Bright-field images were collected using a Nikon Eclipse TE200 microscope (Nikon Instruments). All patient tumor samples were collected after obtaining written informed consent according to the research protocol #18–5005, approved by the University Health Network Research Ethics Board, Toronto, Canada.

For immune cell quantification, a minimum of three regions of interest (ROI) were selected for each condition. Boundaries to outline regions of tumor (Krt5+) were drawn in each image using Qupath (Bankhead et al., 2017), an open source software for digital pathology image analysis, and intratumoral immune cells were counted within these limits. The percentage of intratumoral immune infiltration was calculated as an average of all three ROI.

Flow Cytometry: For flow cytometry of tumor-infiltrating immune cells, harvested tumors were washed with PBS, minced and lysed in Collagenase IV (ThermoFisher) and DNase I (Sigma-Aldrich) for 30 min at 37 degree. Dissociated cells were passed through 70 μm cell strainer. Cells were then washed with PBS, lysed in 1X RBC lysis buffer (Biolegend) and subjected to staining. Surface markers were stained by incubating with antibody cocktails and Live/Dead dye (ThermoFisher) in PBS for 30 mins at room temperature. The following antibodies were used: CD45 Alexa Fluor-700; THY1.2 Alexa Fluor-488; CD4 APC; CD8a PE-Cy7; NK1.1 BV605; and CD11b BV711 (Biolegend) Flow cytometry data was acquired on 5 laser Cytek Aurora (Cytek Biosciences). For flow cytometry measurement of dsRNA, harvested cells were fixed with 4% paraformaldehyde and permeabilized with 90% methanol on ice for 30 min. Cells were washed with PBS and incubated with J2 antibody (SCICONS) at room temperature for 1hr. After washing with PBS and incubating with secondary antibody of Alexa Fluor 488 Goat anti-mouse (ThermoFisher) for 30 min at room temperature in dark, cells were washed with PBS again and analyzed by BD LSR Fortessa Flow Cytometer. For detecting surface expression of IFNLR1, cells were harvested and directly stained with IFNLR1 antibody (Biolegend) or isotype control (Biolegend). Data were acquired on BD LSR Fortessa. All data were analyzed using the FlowJo™ (V10) software.

RNA isolation, quantitative reverse transcription PCR (qRT-PCR) and RNA-sequencing: Total RNA was extracted in TRIzol (Invitrogen) and precipitated in ethanol. For qRT-PCR, cDNA was then synthesized with cDNA Synthesis Kit (Takara) according to the manufacturer's protocols. The relative expression of targeted genes was measured by qRT-PCR with indicated primers and SYBR Green Master Mix (ThermoFisher) using the ABI 7500 Real-Time PCR Detection System (Applied Biosystems). The sequences of primers used are listed in Table S4. For RNA-sequencing, RNA samples were submitted to Columbia University Genome Center for library preparation and sequencing.

RNA-seq data analysis: RNA-seq reads were mapped to the human genome assembly hg38 using HISAT2 (v2.1.0). The mapped reads count of each gene was measured by featureCounts (v1.6.1). The differential gene expression was calculated by the R packages DESeq2 (v1.28.0) and visualized by ggplot2 (v3.2.1). We performed hierarchical clustering on gene expression profiles of samples using the R package pheatmap (Pretty Heatmaps v1.0.10, parameters: clustering_method = 'complete', clustering_distance_cols = 'euclidean'). Gene Ontology (GO) enrichment analysis based on Human Genome Informatics from Gene Ontology Resource knowledgebase (The Gene Ontology, 2019) was performed using Enrichr (https://maayanlab.cloud/Enrichr). Gene set enrichment analyses (GSEA) was performed by using GSEA software (v4.1.0) (Subramanian et al., 2005).

Protein Extraction and Western blot analysis: Whole cell lysates were made in SDS Lysis Buffer (ThermoFisher) and resolved on 3–8% or 4–12% gradient SDS-PAGE gels (ThermoFisher) as previously described (Papillon–Cavanagh et al., 2017).

ELISA: 2'3'-cGAMP ELISA (Cayman) was performed according to manufacturer's protocol. For cell quantification, cells were lysed in M-PER™ Mammalian Protein

Extraction Reagent (Thermo Fisher). Cell lysate from each well was examined according to the manufacturer's instructions.

For IFN-λ2/λ3 ELISA (R&D systems), plate was pre-coated with coating buffer overnight. After 3 washes with 1x Wash Buffer, plate was blocked with 1 x Reagent Dilute at room temperature for 1 hour. Standard samples or culture media from NSD1 WT or KO Cal27 cells were collected and incubated in the plate for 2 hours at room temperature. Plate was then washed 3 times with wash buffer. Detection antibody was diluted in Reagent Dilute and incubated in the plate for 2 hours at room temperature followed by 3 washes. Diluted Streptavidin-HRP B was added to each well and incubated at room temperature for 2 hours. Substrate solution was added and incubated in dark for 20 min. Plate was read at wavelength of 450 nm and 540 nm with a plate reader.

CUT&Tag and ChIP-qPCR: CUT&Tag was performed as described previously (Kaya-Okur et al., 2019). In brief, 1×10^5 cells were washed with 1 ml of wash buffer (20 mM HEPES pH 7.5, 150 mM NaCl, 0.5 mM Spermidine (Sigma-Aldrich), 1× Protease inhibitor cocktail (Sigma-Aldrich)) once. Concanavalin A-coated magnetic beads (Bangs Laboratories) were washed twice with binding buffer (20 mM HEPES pH 7.5, 10 mM KCl, 1 mM $MnCl_2$, 1 mM $CaCl_2$). 10 μl/sample of beads were added to cells and incubated at room temperature for 15 min. Beads-bound cells were resuspended in 100 μl of antibody buffer (20 mM HEPES pH 7.5, 150 mM NaCl, 0.5 mM Spermidine, 0.06% Digitonin (Sigma-Aldrich), 2 mM EDTA, 0.1% BSA, 1× Protease inhibitor cocktail and incubated with indicated antibodies or normal rabbit IgG (Cell Signaling) at 4 degree overnight on nutator. After being washed once with Dig-wash buffer buffer (20 mM HEPES pH 7.5, 150 mM NaCl, 0.5 mM Spermidine, 0.05% Digitonin, 1× Protease inhibitor cocktail), beads-bound cells were incubated with 1 μl Guinea pig anti-rabbit secondary antibody (Antibodies Online) or Donkey anti-Mouse secondary antibody (Sigma-Aldrich) and 2 μl Hyperactive pA-Tn5 Transposase adapter complex in 100 μl Dig-300 buffer (20 mM HEPES•NaOH, pH 7.5, 0.5 mM Spermidine, 1× Protease inhibitor cocktail, 300 mM NaCl, 0.01% Digitonin) at room temperature for 1 h. Cells were washed three times with Dig-300 buffer to remove unbound antibody and Tn5 and then resuspended in 300 μl of tagmentation buffer (10 mM MgCl2 in Dig-300 buffer) and incubated at 37 °C for 1 h. 10 μl of 0.5 M EDTA, 3 μl of 10% SDS and 5 μl of 10 mg ml^{-1} Proteinase K were added to each sample and incubated at 50 °C for 1 h to terminate tagmentation. DNA was purified using PCR purification kit (QIAGEN) and eluted with 25 μl ddH_2O. For library amplification, 21 μl of DNA was mixed with 2μL i5 unique index primer (10 μM), 2 μL i7 unique index primer (10 μM) and 25 μL NEBNext® High-Fidelity 2X PCR Master Mix (NEB) and subjected to the following PCR program: 72°C, 5 min; 98°C, 30 sec; 13 cycles of 98°C, 10 sec and 63°C, 10 sec; 72°C, 1 min and hold at 10°C. To purify the PCR products, 1.1× volumes of pre-warmed Ampure XP beads (Beckman Coulter) were added and incubated at room temperature for 10 min. Libraries were washed twice with 80% ethanol and eluted in 20 μl of 10 mM Tris-HCl, pH 8. Libraries were sequenced on an Illumina NextSeq 550 platform and 75-bp paired-end reads were generated.

ChIP was performed as described previously (Weinberg et al., 2019). In brief, 5×10^6 Cal27 cells were cross-linked with 1% formaldehyde for 5 min at room temperature. 125 mM

Glycine was added to quench the cross-linking reaction. Cells were washed three times with ice-cold PBS and sequentially lysed with 1 mL of LB1 lysis buffer (50mM HEPES-KOH, pH 7.5, 140mM NaCl, 1mM EDTA, 10% glycerol, 0.5% NP-40, 0.25% Triton x-100), 1 mL LB2 lysis buffer (10mM Tris-HCl, pH 8.0, 200mM NaCl, 1mM EDTA, 0.5mM EGTA) for 10 min with rotating. Cells were then resuspended with 130 μl LB3 lysis buffer (10mM Tris-HCl, pH 8.0, 100mM NaCl, 1mM EDTA, 0.5mM EGTA, 0.1% Na-Deoxycholate, 0.5% N-lauroylsarcosine) and transfer to Covaris tubes for 30 min sonication with Covaris Sonicator. 5% of chromatin was saved as input control. H3K27me3 antibody (Cell Signaling) bound to 75 μl of pre-washed Dynabeads (Invitrogen) were added to each sample and incubated at 4 degree overnight. After washing with low salt buffer (150 mM NaCl, 0.1% SDS, 1% Triton X-100, 1 mM EDTA pH 8.0, 50mM Tris HCl pH8.0), high salt buffer (500 mM NaCl, 0.1% SDS, 1% Triton X-100, 1 mM EDTA pH 8.0, 50mM Tris HCl, pH 8.0), LiCl buffer (150mM LiCl, 0.5% Na deoxycholate, 0.1% SDS, 1% NP-40, 1 mM EDTA, pH 8.0, 50mM Tris HCl pH8.0) and TE buffer (10 mM Tris-HCl (pH 8.0), 1 mM EDTA), chromatin was eluted with Elution buffer (1% SDS, 50 mM Tris-HCl, pH 8.0, 10 mM EDTA, 200 mM NaCl) at 65 degree for 30 min and de-crosslinked at 65 degree overnight. RNA and proteins were digested with RNaseA and Proteinase K. DNA was purified with PCR purification kit (QIAGEN). ChIP–qPCR was performed using primers listed in Table S4.

CUT&Tag and ATAC-seq data analysis: CUT&Tag reads were mapped to the human genome assembly hg38 using HISAT2 (v2.1.0). ATAC-seq reads were mapped to the human genome assembly hg38 using HISAT2 (v2.1.0, parameter: -X 2000). Potential PCR duplicates were removed by the function “MarkDuplicates” (parameter: REMOVE_DUPLICATES=true) of Picard (v2.23.1). Peaks of H3K27me3 and H3K36me2 CUT&Tag data were called using SICER2 (parameters: -w 200 -g 2000 -fdr 0.01 for the broad peaks of H3K27me3; -w 10000 -g 30000 -fdr 0.01 for the broad peaks of H3K36me2) with IgG input as control. The H3K27me3 peaks are mapped to promoter regions by the function “map” of bedtools (v2.27.1). The reads counts of H3K36me2 and H3K27me3 CUT&Tag data in H3K36me2 broad peaks were measured by featureCounts (v1.6.1). Genomic enrichment of CUT&Tag and ATAC-seq signals were visualized using IGV.

Estimation of immune infiltration in SCC samples: Transcriptome, DNA methylation, copy number variation, retrotransposition, structural variation and genetic mutation profiles of TCGA tumor samples were downloaded from cBioportal (https://www.cbioportal.org) (Cerami et al., 2012). Estimated leukocyte fraction scores of TCGA tumor samples were calculated based on their transcriptome and DNA methylation signatures as previously described (Taylor et al., 2018). Cell type classification was aggregated for each HNSCC sample based on published single-cell RNA-sequencing dataset (Puram et al., 2017). Tumor IMmune Estimation Resource (TIMER) scores of TCGA HNSC tumor samples were calculated based on their transcriptome signatures (Li et al., 2016).

Supplementary Material

Refer to Web version on PubMed Central for supplementary material.

ACKNOWLEDGEMENTS

We thank members of the Lu lab for critical reading of the manuscript. We thank Chavez lab for the technical support of CRISPRa experiment. This research was supported by US National Institutes of Health (NIH) grants (P01CA196539 to C.L. and J.M.; R01DK132251 to C.L. and J.Q.; R01DE031873, R01CA266978 and R35GM138181 to C.L.; NCI Cancer Center Support Grant P30CA013696) and funding from the Concern foundation (to C.L.). C.L. acknowledges support from the Pew-Stewart Scholars for Cancer Research Award. B.I. acknowledges support from NIH (R37CA258829 and R21CA263381) and Burroughs Wellcome Fund Career Award for Medical Scientists. A.C. acknowledges support from NIH (R01CA197774 and R01CA227450) and the Pershing Square Sohn Cancer Research Award. Flow cytometry analysis and cell sorting were performed in the CCTI Flow Cytometry Core, supported in part by the Office of the Director, National Institutes of Health under awards S10OD020056. Schematic diagrams were created using BioRender.

REFERENCE

Anzalone AV, Randolph PB, Davis JR, Sousa AA, Koblan LW, Levy JM, Chen PJ, Wilson C, Newby GA, Raguram A, et al. (2019). Search-and-replace genome editing without double-strand breaks or donor DNA. Nature 576, 149–157. [PubMed: 31634902]

Bankhead P, Loughrey MB, Fernandez JA, Dombrowski Y, McArt DG, Dunne PD, McQuaid S, Gray RT, Murray LJ, Coleman HG, et al. (2017). QuPath: Open source software for digital pathology image analysis. Sci Rep 7, 16878. [PubMed: 29203879]

Bates SE (2020). Epigenetic Therapies for Cancer. N Engl J Med 383, 650–663. [PubMed: 32786190]

Blanpain C, and Fuchs E (2006). Epidermal stem cells of the skin. Annu Rev Cell Dev Biol 22, 339–373. [PubMed: 16824012]

Brennan K, Shin JH, Tay JK, Prunello M, Gentles AJ, Sunwoo JB, and Gevaert O (2017). NSD1 inactivation defines an immune cold, DNA hypomethylated subtype in squamous cell carcinoma. Sci Rep 7, 17064. [PubMed: 29213088]

Burr ML, Sparbier CE, Chan KL, Chan YC, Kersbergen A, Lam EYN, Azidis-Yates E, Vassiliadis D, Bell CC, Gilan O, et al. (2019). An Evolutionarily Conserved Function of Polycomb Silences the MHC Class I Antigen Presentation Pathway and Enables Immune Evasion in Cancer. Cancer Cell 36, 385–401 e388. [PubMed: 31564637]

Campbell JD, Yau C, Bowlby R, Liu Y, Brennan K, Fan H, Taylor AM, Wang C, Walter V, Akbani R, et al. (2018). Genomic, Pathway Network, and Immunologic Features Distinguishing Squamous Carcinomas. Cell Rep 23, 194–212 e196. [PubMed: 29617660]

Cancer Genome Atlas N (2015). Comprehensive genomic characterization of head and neck squamous cell carcinomas. Nature 517, 576–582. [PubMed: 25631445]

Cerami E, Gao J, Dogrusoz U, Gross BE, Sumer SO, Aksoy BA, Jacobsen A, Byrne CJ, Heuer ML, Larsson E, et al. (2012). The cBio cancer genomics portal: an open platform for exploring multidimensional cancer genomics data. Cancer Discov 2, 401–404. [PubMed: 22588877]

Chavez A, Scheiman J, Vora S, Pruitt BW, Tuttle M, E PRI, Lin S, Kiani S, Guzman CD, Wiegand DJ, et al. (2015). Highly efficient Cas9-mediated transcriptional programming. Nat Methods 12, 326–328. [PubMed: 25730490]

Chiappinelli KB, Strissel PL, Desrichard A, Li H, Henke C, Akman B, Hein A, Rote NS, Cope LM, Snyder A, et al. (2015). Inhibiting DNA Methylation Causes an Interferon Response in Cancer via dsRNA Including Endogenous Retroviruses. Cell 162, 974–986. [PubMed: 26317466]

Chiappinelli KB, Zahnow CA, Ahuja N, and Baylin SB (2016). Combining Epigenetic and Immunotherapy to Combat Cancer. Cancer Res 76, 1683–1689. [PubMed: 26988985]

Corces MR, Granja JM, Shams S, Louie BH, Seoane JA, Zhou W, Silva TC, Groeneveld C, Wong CK, Cho SW, et al. (2018). The chromatin accessibility landscape of primary human cancers. Science 362.

Ennishi D, Takata K, Beguelin W, Duns G, Mottok A, Farinha P, Bashashati A, Saberi S, Boyle M, Meissner B, et al. (2019). Molecular and Genetic Characterization of MHC Deficiency Identifies EZH2 as Therapeutic Target for Enhancing Immune Recognition. Cancer Discov 9, 546–563. [PubMed: 30705065]

Farhangdoost N, Horth C, Hu B, Bareke E, Chen X, Li Y, Coradin M, Garcia BA, Lu C, and Majewski J (2021). Chromatin dysregulation associated with NSD1 mutation in head and neck squamous cell carcinoma. Cell Rep 34, 108769. [PubMed: 33626351]

Ferris RL, Blumenschein G Jr., Fayette J, Guigay J, Colevas AD, Licitra L, Harrington K, Kasper S, Vokes EE, Even C, et al. (2016). Nivolumab for Recurrent Squamous-Cell Carcinoma of the Head and Neck. N Engl J Med 375, 1856–1867. [PubMed: 27718784]

Gao J, Shi LZ, Zhao H, Chen J, Xiong L, He Q, Chen T, Roszik J, Bernatchez C, Woodman SE, et al. (2016). Loss of IFN-gamma Pathway Genes in Tumor Cells as a Mechanism of Resistance to Anti-CTLA-4 Therapy. Cell 167, 397–404 e399. [PubMed: 27667683]

Goswami S, Apostolou I, Zhang J, Skepner J, Anandhan S, Zhang X, Xiong L, Trojer P, Aparicio A, Subudhi SK, et al. (2018). Modulation of EZH2 expression in T cells improves efficacy of anti-CTLA-4 therapy. J Clin Invest 128, 3813–3818. [PubMed: 29905573]

Gray SM, Amezquita RA, Guan T, Kleinstein SH, and Kaech SM (2017). Polycomb Repressive Complex 2-Mediated Chromatin Repression Guides Effector CD8(+) T Cell Terminal Differentiation and Loss of Multipotency. Immunity 46, 596–608. [PubMed: 28410989]

He S, Liu Y, Meng L, Sun H, Wang Y, Ji Y, Purushe J, Chen P, Li C, Madzo J, et al. (2017). Ezh2 phosphorylation state determines its capacity to maintain CD8(+) T memory precursors for antitumor immunity. Nat Commun 8, 2125. [PubMed: 29242551]

Indra AK, Warot X, Brocard J, Bornert JM, Xiao JH, Chambon P, and Metzger D (1999). Temporally-controlled site-specific mutagenesis in the basal layer of the epidermis: comparison of the recombinase activity of the tamoxifen-inducible Cre-ER(T) and Cre-ER(T2) recombinases. Nucleic Acids Res 27, 4324–4327. [PubMed: 10536138]

Johnson DE, Burtness B, Leemans CR, Lui VWY, Bauman JE, and Grandis JR (2020). Head and neck squamous cell carcinoma. Nat Rev Dis Primers 6, 92. [PubMed: 33243986]

Jones PA (2012). Functions of DNA methylation: islands, start sites, gene bodies and beyond. Nat Rev Genet 13, 484–492. [PubMed: 22641018]

Jones PA, Ohtani H, Chakravarthy A, and De Carvalho DD (2019). Epigenetic therapy in immune-oncology. Nat Rev Cancer 19, 151–161. [PubMed: 30723290]

Judd NP, Allen CT, Winkler AE, and Uppaluri R (2012a). Comparative analysis of tumor-infiltrating lymphocytes in a syngeneic mouse model of oral cancer. Otolaryngol Head Neck Surg 147, 493–500. [PubMed: 22434099]

Judd NP, Winkler AE, Murillo-Sauca O, Brotman JJ, Law JH, Lewis JS Jr., Dunn GP, Bui JD, Sunwoo JB, and Uppaluri R (2012b). ERK1/2 regulation of CD44 modulates oral cancer aggressiveness. Cancer Res 72, 365–374. [PubMed: 22086849]

Jung H, Kim HS, Kim JY, Sun JM, Ahn JS, Ahn MJ, Park K, Esteller M, Lee SH, and Choi JK (2019). DNA methylation loss promotes immune evasion of tumours with high mutation and copy number load. Nat Commun 10, 4278. [PubMed: 31537801]

Kato S, Weng QY, Insco ML, Chen KY, Muralidhar S, Pozniak J, Diaz JMS, Drier Y, Nguyen N, Lo JA, et al. (2020). Gain-of-Function Genetic Alterations of G9a Drive Oncogenesis. Cancer Discov 10, 980–997. [PubMed: 32269030]

Kawai T, and Akira S (2010). The role of pattern-recognition receptors in innate immunity: update on Toll-like receptors. Nat Immunol 11, 373–384. [PubMed: 20404851]

Kaya-Okur HS, Wu SJ, Codomo CA, Pledger ES, Bryson TD, Henikoff JG, Ahmad K, and Henikoff S (2019). CUT&Tag for efficient epigenomic profiling of small samples and single cells. Nat Commun 10, 1930. [PubMed: 31036827]

Kotenko SV, Gallagher G, Baurin VV, Lewis-Antes A, Shen M, Shah NK, Langer JA, Sheikh F, Dickensheets H, and Donnelly RP (2003). IFN-lambdas mediate antiviral protection through a distinct class II cytokine receptor complex. Nat Immunol 4, 69–77. [PubMed: 12483210]

Li B, Severson E, Pignon JC, Zhao H, Li T, Novak J, Jiang P, Shen H, Aster JC, Rodig S, et al. (2016). Comprehensive analyses of tumor immunity: implications for cancer immunotherapy. Genome Biol 17, 174. [PubMed: 27549193]

Li J, Wang W, Zhang Y, Cieslik M, Guo J, Tan M, Green MD, Wang W, Lin H, Li W, et al. (2020). Epigenetic driver mutations in ARID1A shape cancer immune phenotype and immunotherapy. J Clin Invest 130, 2712–2726. [PubMed: 32027624]

Liu H, Golji J, Brodeur LK, Chung FS, Chen JT, deBeaumont RS, Bullock CP, Jones MD, Kerr G, Li L, et al. (2019). Tumor-derived IFN triggers chronic pathway agonism and sensitivity to ADAR loss. Nat Med 25, 95–102. [PubMed: 30559422]

Liu XD, Kong W, Peterson CB, McGrail DJ, Hoang A, Zhang X, Lam T, Pilie PG, Zhu H, Beckermann KE, et al. (2020). PBRM1 loss defines a nonimmunogenic tumor phenotype associated with checkpoint inhibitor resistance in renal carcinoma. Nat Commun 11, 2135. [PubMed: 32358509]

Lu C, Ward PS, Kapoor GS, Rohle D, Turcan S, Abdel-Wahab O, Edwards CR, Khanin R, Figueroa ME, Melnick A, et al. (2012). IDH mutation impairs histone demethylation and results in a block to cell differentiation. Nature 483, 474–478. [PubMed: 22343901]

Lu T, Jackson MW, Wang B, Yang M, Chance MR, Miyagi M, Gudkov AV, and Stark GR (2010). Regulation of NF-kappaB by NSD1/FBXL11-dependent reversible lysine methylation of p65. Proc. Natl. Acad. Sci. U.S.A 107, 46–51. [PubMed: 20080798]

Mackenzie KJ, Carroll P, Martin CA, Murina O, Fluteau A, Simpson DJ, Olova N, Sutcliffe H, Rainger JK, Leitch A, et al. (2017). cGAS surveillance of micronuclei links genome instability to innate immunity. Nature 548, 461–465. [PubMed: 28738408]

Marango J, Shimoyama M, Nishio H, Meyer JA, Min DJ, Sirulnik A, Martinez-Martinez Y, Chesi M, Bergsagel PL, Zhou MM, et al. (2008). The MMSET protein is a histone methyltransferase with characteristics of a transcriptional corepressor. Blood 111, 3145–3154. [PubMed: 18156491]

Marcello T, Grakoui A, Barba-Spaeth G, Machlin ES, Kotenko SV, MacDonald MR, and Rice CM (2006). Interferons alpha and lambda inhibit hepatitis C virus replication with distinct signal transduction and gene regulation kinetics. Gastroenterology 131, 1887–1898. [PubMed: 17087946]

Morel KL, Sheahan AV, Burkhart DL, Baca SC, Boufaied N, Liu Y, Qiu X, Canadas I, Roehle K, Heckler M, et al. (2021). EZH2 inhibition activates a dsRNA-STING-interferon stress axis that potentiates response to PD-1 checkpoint blockade in prostate cancer. Nat Cancer 2, 444–456. [PubMed: 33899001]

Nauta JM, Roodenburg JL, Nikkels PG, Witjes MJ, and Vermey A (1995). Comparison of epithelial dysplasia--the 4NQO rat palate model and human oral mucosa. Int J Oral Maxillofac Surg 24, 53–58. [PubMed: 7782642]

Papillon-Cavanagh S, Lu C, Gayden T, Mikael LG, Bechet D, Karamboulas C, Ailles L, Karamchandani J, Marchione DM, Garcia BA, et al. (2017). Impaired H3K36 methylation defines a subset of head and neck squamous cell carcinomas. Nat Genet 49, 180–185. [PubMed: 28067913]

Puram SV, Tirosh I, Parikh AS, Patel AP, Yizhak K, Gillespie S, Rodman C, Luo CL, Mroz EA, Emerick KS, et al. (2017). Single-Cell Transcriptomic Analysis of Primary and Metastatic Tumor Ecosystems in Head and Neck Cancer. Cell 171, 1611–1624 e1624. [PubMed: 29198524]

Qing Y, Dong L, Gao L, Li C, Li Y, Han L, Prince E, Tan B, Deng X, Wetzel C, et al. (2021). R-2-hydroxyglutarate attenuates aerobic glycolysis in leukemia by targeting the FTO/m6A/PFKP/LDHB axis. Molecular Cell 81, 922–939.e9. [PubMed: 33434505]

Rodriguez-Martin B, Alvarez EG, Baez-Ortega A, Zamora J, Supek F, Demeulemeester J, Santamarina M, Ju YS, Temes J, Garcia-Souto D, et al. (2020). Pan-cancer analysis of whole genomes identifies driver rearrangements promoted by LINE-1 retrotransposition. Nat Genet 52, 306–319. [PubMed: 32024998]

Roulois D, Loo Yau H, Singhania R, Wang Y, Danesh A, Shen SY, Han H, Liang G, Jones PA, Pugh TJ, et al. (2015). DNA-Demethylating Agents Target Colorectal Cancer Cells by Inducing Viral Mimicry by Endogenous Transcripts. Cell 162, 961–973. [PubMed: 26317465]

Sadler AJ, and Williams BR (2008). Interferon-inducible antiviral effectors. Nat Rev Immunol 8, 559–568. [PubMed: 18575461]

Shen H, and Laird PW (2013). Interplay between the cancer genome and epigenome. Cell 153, 38–55. [PubMed: 23540689]

Shen J, Ju Z, Zhao W, Wang L, Peng Y, Ge Z, Nagel ZD, Zou J, Wang C, Kapoor P, et al. (2018). ARID1A deficiency promotes mutability and potentiates therapeutic antitumor immunity unleashed by immune checkpoint blockade. Nat Med 24, 556–562. [PubMed: 29736026]

Sheppard P, Kindsvogel W, Xu W, Henderson K, Schlutsmeyer S, Whitmore TE, Kuestner R, Garrigues U, Birks C, Roraback J, et al. (2003). IL-28, IL-29 and their class II cytokine receptor IL-28R. Nat Immunol 4, 63–68. [PubMed: 12469119]

Shin DS, Zaretsky JM, Escuin-Ordinas H, Garcia-Diaz A, Hu-Lieskovan S, Kalbasi A, Grasso CS, Hugo W, Sandoval S, Torrejon DY, et al. (2017). Primary Resistance to PD-1 Blockade Mediated by JAK1/2 Mutations. Cancer Discov 7, 188–201. [PubMed: 27903500]

Shirane K, Miura F, Ito T, and Lorincz MC (2020). NSD1-deposited H3K36me2 directs de novo methylation in the mouse male germline and counteracts Polycomb-associated silencing. Nat Genet 52, 1088–1098. [PubMed: 32929285]

Streubel G, Watson A, Jammula SG, Scelfo A, Fitzpatrick DJ, Oliviero G, McCole R, Conway E, Glancy E, Negri GL, et al. (2018). The H3K36me2 Methyltransferase Nsd1 Demarcates PRC2-Mediated H3K27me2 and H3K27me3 Domains in Embryonic Stem Cells. Mol Cell 70, 371–379 e375. [PubMed: 29606589]

Subramanian A, Tamayo P, Mootha VK, Mukherjee S, Ebert BL, Gillette MA, Paulovich A, Pomeroy SL, Golub TR, Lander ES, et al. (2005). Gene set enrichment analysis: a knowledge-based approach for interpreting genome-wide expression profiles. Proc Natl Acad Sci U S A 102, 15545–15550. [PubMed: 16199517]

Taylor AM, Shih J, Ha G, Gao GF, Zhang X, Berger AC, Schumacher SE, Wang C, Hu H, Liu J, et al. (2018). Genomic and Functional Approaches to Understanding Cancer Aneuploidy. Cancer Cell 33, 676–689 e673. [PubMed: 29622463]

The Gene Ontology C (2019). The Gene Ontology Resource: 20 years and still GOing strong. Nucleic Acids Res 47, D330–D338. [PubMed: 30395331]

Thorsson V, Gibbs DL, Brown SD, Wolf D, Bortone DS, Ou Yang TH, Porta-Pardo E, Gao GF, Plaisier CL, Eddy JA, et al. (2018). The Immune Landscape of Cancer. Immunity 48, 812–830 e814. [PubMed: 29628290]

Wang Z, Wu VH, Allevato MM, Gilardi M, He Y, Luis Callejas-Valera J, Vitale-Cross L, Martin D, Amornphimoltham P, McDermott J, et al. (2019). Syngeneic animal models of tobacco-associated oral cancer reveal the activity of in situ anti-CTLA-4. Nat Commun 10, 5546. [PubMed: 31804466]

Weinberg DN, Papillon-Cavanagh S, Chen H, Yue Y, Chen X, Rajagopalan KN, Horth C, McGuire JT, Xu X, Nikbakht H, et al. (2019). The histone mark H3K36me2 recruits DNMT3A and shapes the intergenic DNA methylation landscape. Nature 573, 281–286. [PubMed: 31485078]

Xu W, Li J, Rong B, Zhao B, Wang M, Dai R, Chen Q, Liu H, Gu Z, Liu S, et al. (2020). DNMT3A reads and connects histone H3K36me2 to DNA methylation. Protein Cell 11, 150–154. [PubMed: 31758527]

Ye L, Schnepf D, and Staeheli P (2019). Interferon-lambda orchestrates innate and adaptive mucosal immune responses. Nat Rev Immunol 19, 614–625. [PubMed: 31201377]

Yuan W, Xu M, Huang C, Liu N, Chen S, and Zhu B (2011). H3K36 methylation antagonizes PRC2-mediated H3K27 methylation. J Biol Chem 286, 7983–7989. [PubMed: 21239496]

Zaretsky JM, Garcia-Diaz A, Shin DS, Escuin-Ordinas H, Hugo W, Hu-Lieskovan S, Torrejon DY, Abril-Rodriguez G, Sandoval S, Barthly L, et al. (2016). Mutations Associated with Acquired Resistance to PD-1 Blockade in Melanoma. N Engl J Med 375, 819–829. [PubMed: 27433843]

Zhou L, Mudianto T, Ma X, Riley R, and Uppaluri R (2020). Targeting EZH2 Enhances Antigen Presentation, Antitumor Immunity, and Circumvents Anti-PD-1 Resistance in Head and Neck Cancer. Clin Cancer Res 26, 290–300. [PubMed: 31562203]

Zhou W, Dinh HQ, Ramjan Z, Weisenberger DJ, Nicolet CM, Shen H, Laird PW, and Berman BP (2018). DNA methylation loss in late-replicating domains is linked to mitotic cell division. Nat Genet 50, 591–602. [PubMed: 29610480]

Highlights

- *NSD1* mutant SCCs show retrotransposon de-repression yet an immune cold phenotype
- NSD1 loss drives tumor immune evasion in syngeneic and genetic mouse models of SCC
- NSD1 loss silences tumor interferon response genes through increased H3K27me3
- EZH2 inhibitor restores immune infiltration and impairs *Nsd1* mutant tumor growth

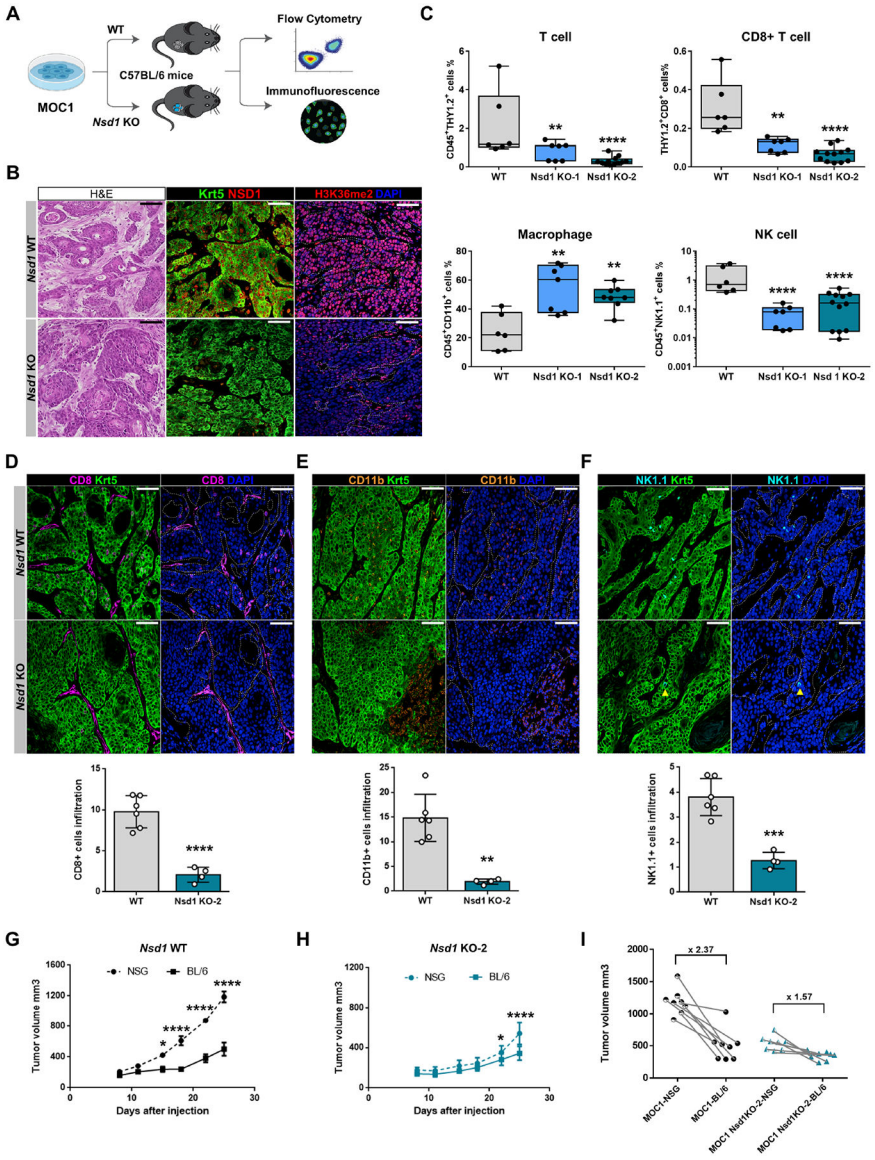

Figure 1: NSD1 loss reduces tumor immune infiltration in syngeneic HNSCC mouse model.

A, Schematic illustrating the implantation of *Nsd1* wildtype (WT) or knockout (KO) MOC1 cells into C57BL/6 mice and tumor immune microenvironment analysis.

B, Representative Hematoxylin and eosin (H&E) staining and immunofluorescent staining of keratin 5 (KRT5), NSD1 and H3K36me2 in *Nsd1* WT or KO MOC1 tumors.

C, Percentage of intra-tumoral T cells, CD8+ T cells, natural killer (NK) cells and macrophages determined by multi-channel flow cytometry from subcutaneously injected *Nsd1* WT or KO MOC1 tumors (n = 6–10). Scale bar, 50 μm.

D-F, Representative immunofluorescent staining of KRT5 and CD8+ T cells (D), CD11b+ macrophages (E) and NK1.1+ natural killer (NK) cells (F) in *Nsd1* WT or KO MOC1 tumors. Bar graphs below show the average % immune infiltration into the Krt5+ tumor compartment from at least three regions of interest (ROI) per mouse, quantified for each

immune cell type (4–6 mice per group; two-sided Student's test; data are represented as mean ± SD). Scale bar, 50 μm.

G-H, Volumes of *Nsd1* wildtype (WT) (G) or knockout (KO) MOC1 (H) tumors in NSG mice or C57BL/6 mice. Data represent mean ± SEM. n=8 per group.

I, Comparison of wildtype and *Nsd1* knockout (KO) MOC1 tumor volume in C57BL/6 mice and NSG mice in (G) and (H) at day 25 after injection.

*, $p<0.05$, **, $p<0.01$, ***, $p<0.001$, ****, $p<0.0001$.

See also Figure S1.

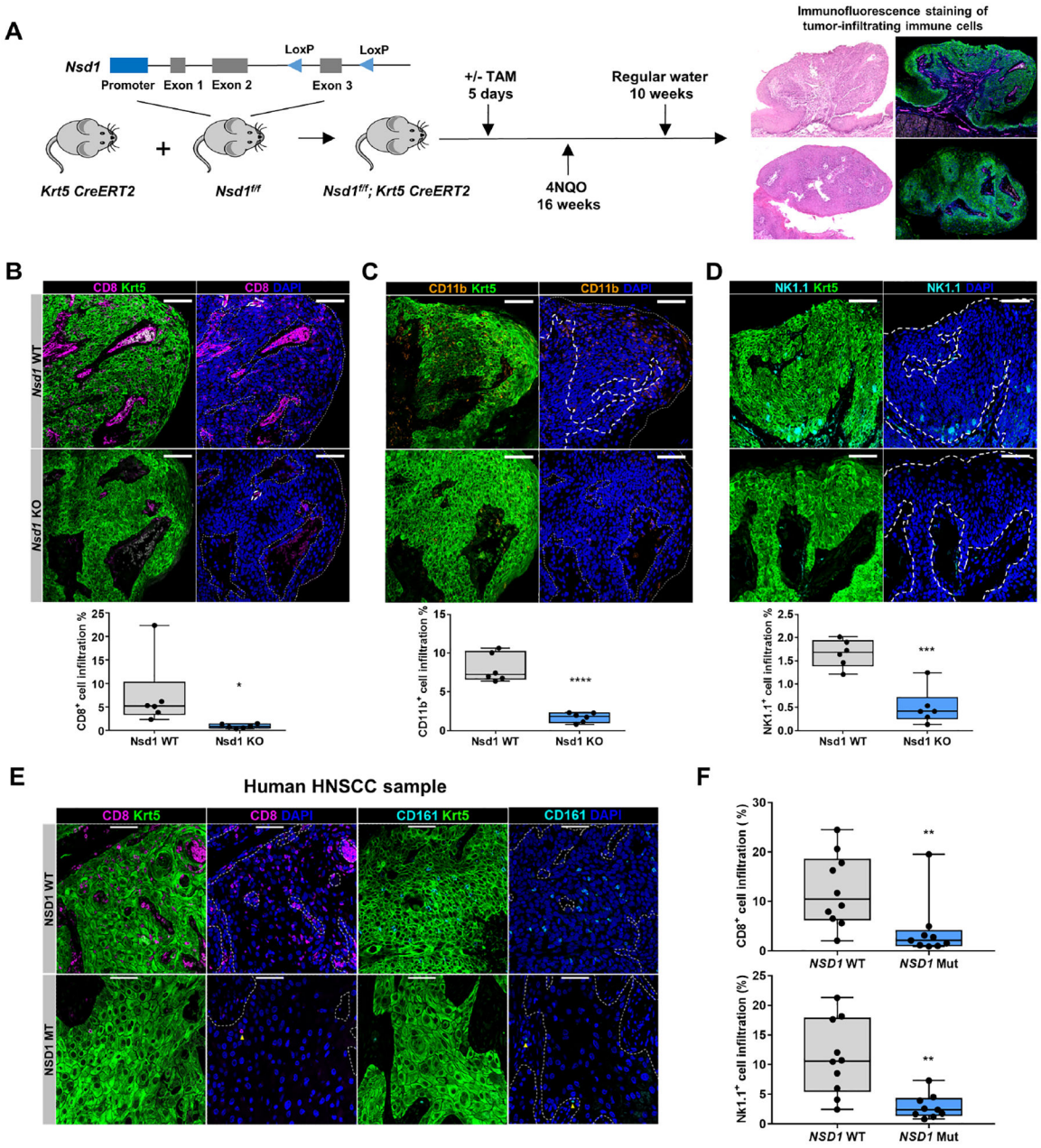

Figure 2: Ablation of *Nsd1* induces immune-cold phenotype in a model of carcinogen-induced oral SCC.

A, Left, schematic illustrating the generation of *Nsd1* conditional knockout mice and development of primary oral lesions induced by 4NQO. Right: H&E staining and immunofluorescent images of tongue lesions at the 26-week time point from control (top) and *Nsd1*-KO mice (bottom).

B-D, Representative immunofluorescent staining of keratin 5 (KRT5) and CD8+ T cells (B), CD11b+ macrophages (C) and NK1.1+ natural killer (NK) cells (D) in carcinogen-induced tongue lesions from *Nsd1* wildtype (WT) mice (top) and *Nsd1* knockout (KO) mice (bottom). Bar graphs below show the average % immune infiltration into the Krt5+ tumor compartment from at least three regions of interest (ROI) per lesion, quantified for each

immune cell type (5–6 mice per group; two-sided Student's test; data are represented as mean ± SD). Scale bar, 100 μm.

E, Representative immunofluorescent staining of Krt5, CD8+ T cells and CD161+ NK cells in primary human HNSCC samples highlighting reduced abundance of immune cells (yellow arrowheads) in *NSD1* mutant (MT) compared to wildtype (WT) tumors. Scale bar, 50 μm.

F, Quantification of at least three regions of interest (ROI) per human sample reveals reduced CD8+ T cell and NK cell infiltration into human *NSD1* mutant (Mut) tumors (Krt5+ compartment) (n=10 for *NSD1* WT patient samples, n=9 for *NSD1* Mut patient samples; two-sided Student's test; data are represented as mean ± SD). Patient characteristics are listed in Table S1.

*, $p<0.05$; **, $p<0.01$, ***, $p<0.001$, ****, $p<0.0001$.

See also Figure S2 and Table S1.

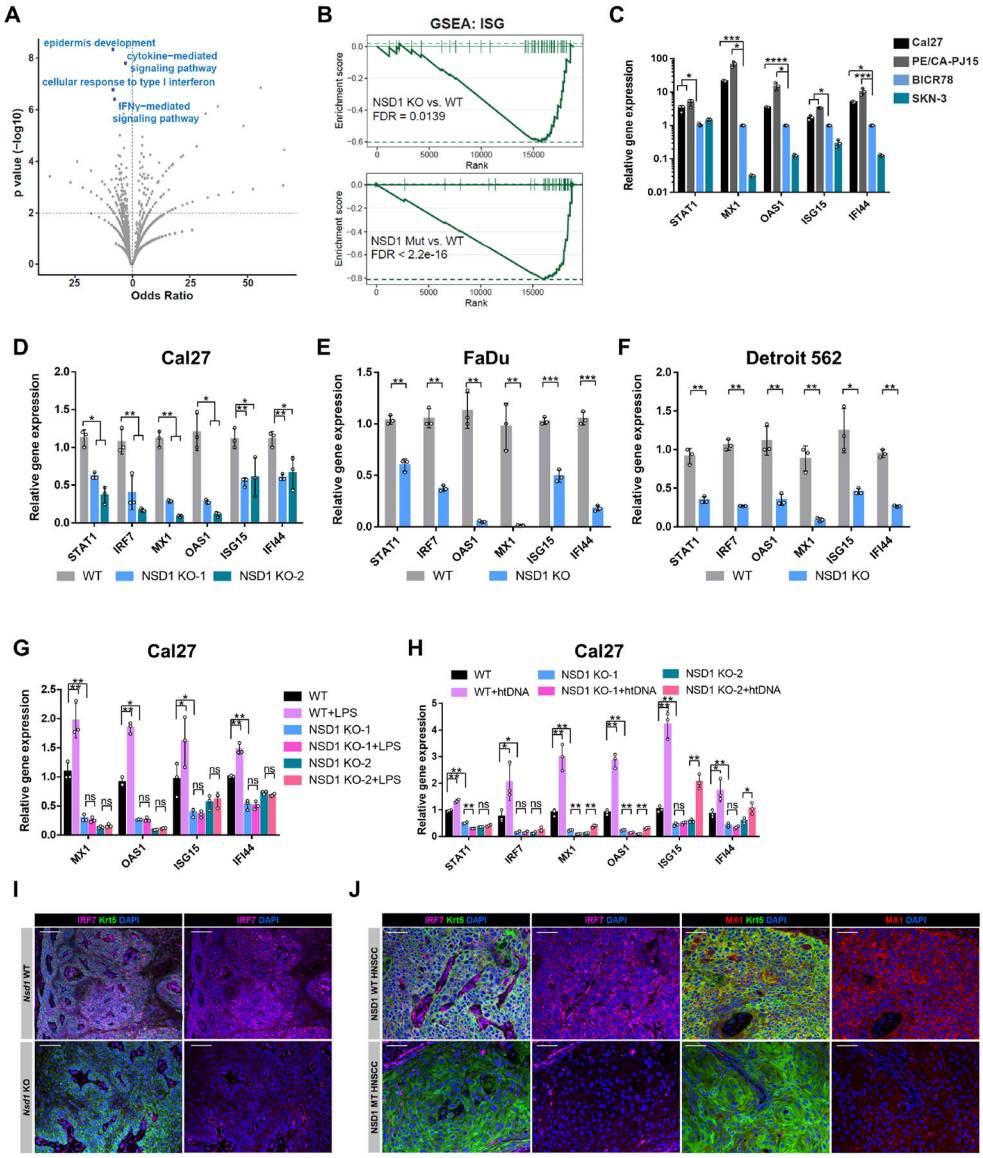

Figure 3: NSD1 loss decreases the expression of interferon-stimulated genes.

A, Gene ontology (GO) analysis of differentially expressed genes between *NSD1* wildtype and knockout Cal27 cells. The top statistically significantly enriched GO groups among downregulated genes in *NSD1* knockout cells are highlighted in blue.

B, Gene set enrichment analysis (GSEA) showing interferon-stimulated genes (ISGs) are significantly enriched among downregulated genes in *NSD1* knockout (KO) Cal27 cells (top) or *NSD1* mutant (Mut) SKN-3 and BICR78 cells (bottom) versus wildtype (WT) Cal27 cells.

C, qRT-PCR analysis of *STAT1* and representative ISGs in *NSD1* wildtype (Cal27 and PE/CA-PJ15) or mutant (BICR78 and SKN-3) HNSCC cells. Data represent mean ± SD, n=3.

D-F, qRT-PCR analysis of *STAT1* and representative ISGs comparing *NSD1* knockout (KO) to wildtype (WT) Cal27 (D), Fadu (E) or Detroit 562 (F) HNSCC cells. Data represent mean ± SD, n=3.

G, qRT-PCR analysis of representative ISGs in *NSD1* knockout (KO) or wildtype (WT) Cal27 cells with or without 10 μg/mL Lipopolysaccharide (LPS) treatment for 24 hrs. Data represent mean ± SD, n=3.

H, qRT-PCR analysis of representative ISGs in *NSD1* knockout (KO) or wildtype (WT) Cal27 cells with or without transfecting with 1 μg/mL herring testis DNA (htDNA) for 5 hrs. Data represent mean ± SD, n=3.

I, Representative immunofluorescent staining of KRT5 and IRF7 in carcinogen-induced tongue lesions from *Nsd1* wildtype (WT) mice (top) and *Nsd1* knockout (KO) mice (bottom). Scale bar, 50 μm.

J, Representative immunofluorescent staining of KRT5 and IRF7 or MX1 in *NSD1* wildtype (WT) or *NSD1* mutant (MT) human HNSCC patient samples.

*, $p<0.05$; **, $p<0.01$, ***, $p<0.001$, ****, $p<0.0001$. Scale bar, 50 μm.

See also Figure S3.

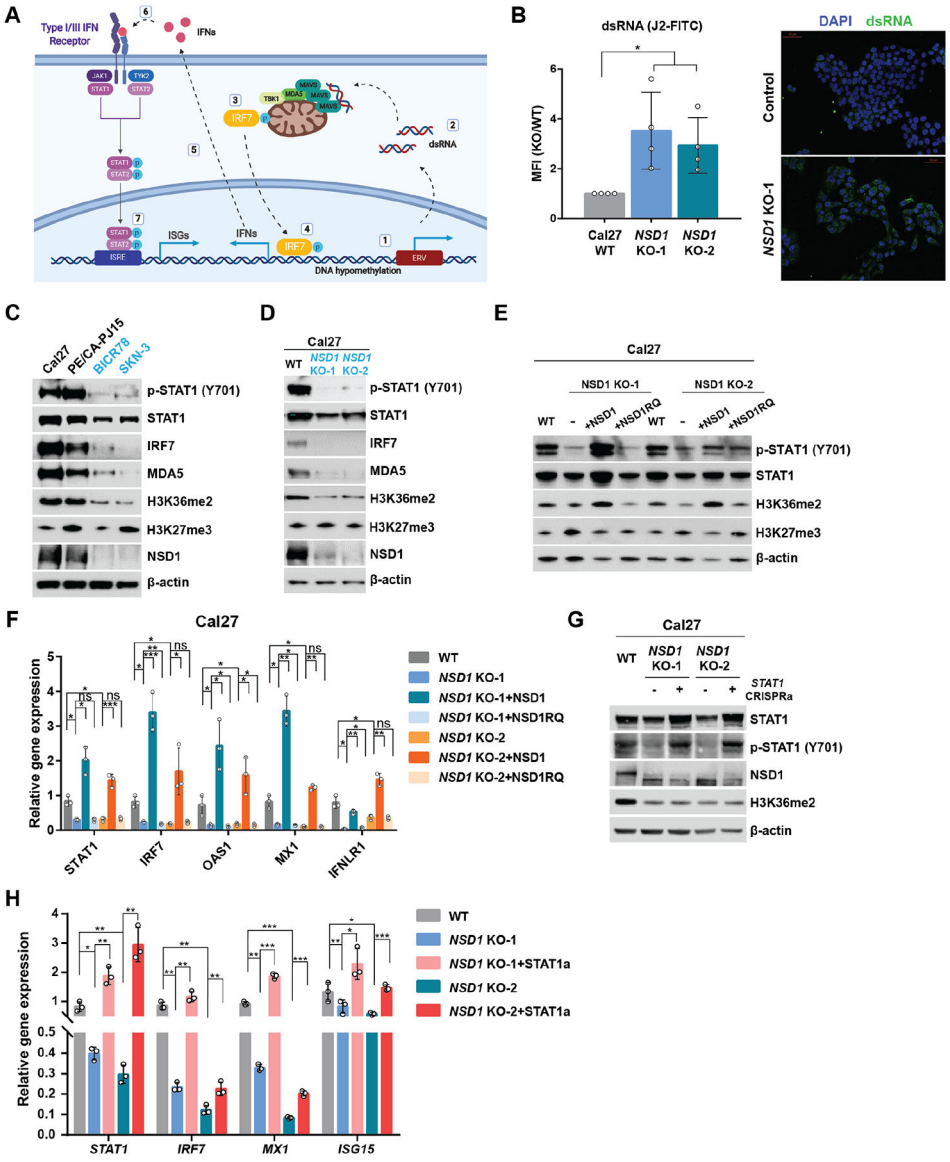

Figure 4: NSD1 loss impairs interferon signaling response.

A, Schematic view of dsRNA production, sensing and the downstream type I & III interferon response pathways.

B, *NSD1* wildtype (WT) or knockout (KO) Cal27 cells were stained with J2 antibody (anti-dsRNA) and subjected to flow cytometry quantification (left) or immunofluorescence staining (right). Data represent mean ± SD of fold increase of mean fluorescence intensity (MFI) in *NSD1* knockout (KO) Cal27 cells versus in *NSD1* wildtype (WT) Cal27 cells, n=4.

C, Western blots showing expression of interferon pathway proteins in *NSD1* wildtype (Cal27, PE/CA-PJ15) or mutant (BICR78, SKN-3) HNSCC cells.

D, Western blots showing expression of interferon pathway proteins in *NSD1* wildtype (WT) or knockout (KO) Cal27 cells.

E, Western blots showing STAT1 expression and phosphorylation in *NSD1* wildtype (WT), *NSD1* knockout (KO) Cal27 cells and KO cells with ectopic expression of truncated wildtype or catalytic-dead R2017Q mutant NSD1 (NSD1RQ).
F, qRT-PCR analysis of *STAT1* and representative ISGs in cell lines listed in (E). Data represent mean ± SD, n=3.
G, Western blots showing increased STAT1 expression and phosphorylation by CRISPR activation in Cal27 *NSD1* knockout (KO) cells.
H, qRT-PCR analysis of representative ISGs in Cal27 wildtype (WT) and *NSD1* knockout (KO) cells with or without STAT1 activation. Data represent mean ± SD, n=3.
*, $p<0.05$; **, $p<0.01$, ***, $p<0.001$, ns, not significant.
See also Figure S4.

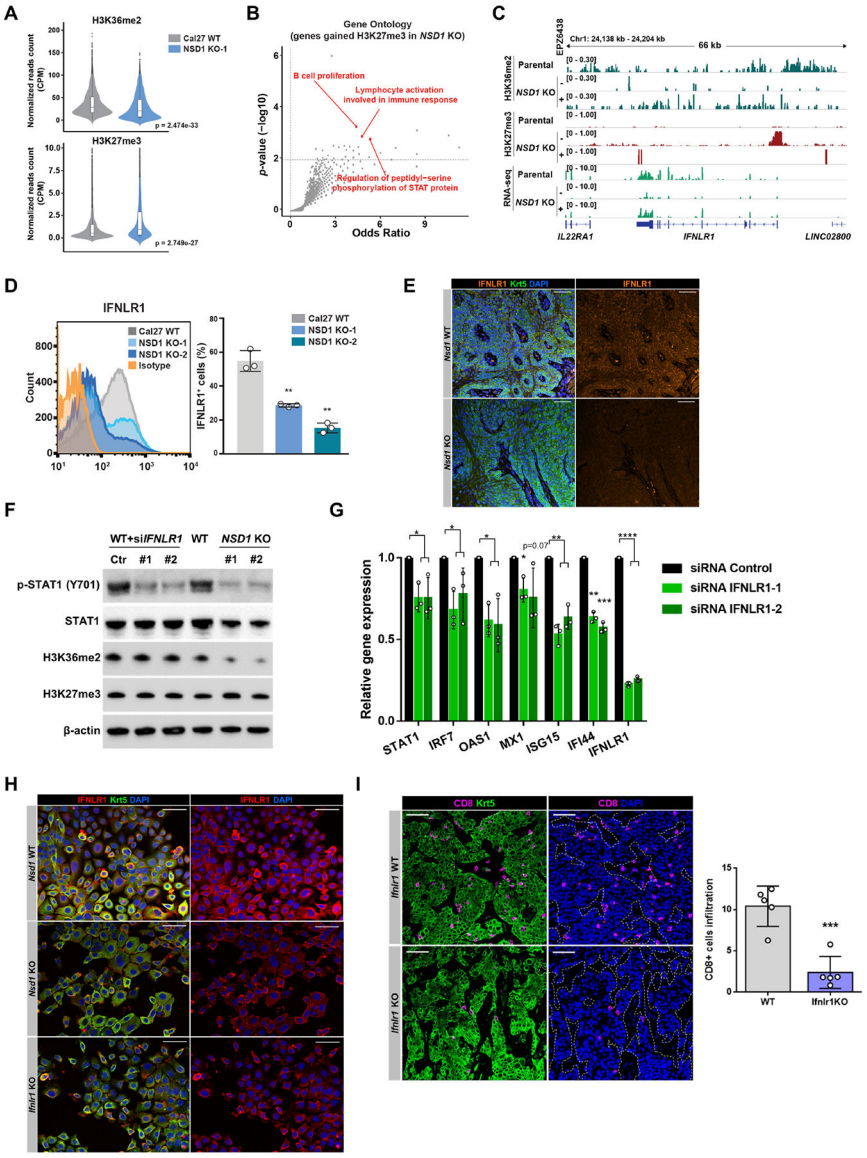

Figure 5: Epigenetic silencing of IFNLR1 contributes to NSD1 loss-induced immune evasion.

A, Violin plots showing the global levels of H3K36me2 and H3K27me3 (counts per million of CUT&Tag reads) in *NSD1* wildtype (WT) or knockout (KO) Cal27 cells. Bin size = 10 Mb. The center line in the embedded boxplots represents the median, the box limits are the 25th and 75th percentiles, and the whiskers are the minimum to maximum values. P-values were determined by two-tailed Student's t-test.

B, Gene ontology (GO) analysis of genes that gained H3K27me3 in *NSD1* knockout (KO) Cal27 cells. The top statistically significantly enriched GO groups are highlighted in red.

C, IGV snapshot showing the chromatin landscape of H3K36me2, H3K27me3, and gene transcription at the *IFNLR1* locus in wildtype or *NSD1* knockout (KO) Cal27 cells with or without the treatment of 3 μM EPZ-6438 for 10 days.

D, Flow cytometry analysis of cell surface expression of IFNLR1 in *NSD1* wildtype (WT) or knockout (KO) Cal27 cells. The percentage of IFNLR1-positive cells is shown as bar graph. Data represent mean ± SD, n=3.

E, Representative immunofluorescent staining of KRT5 and IFNLR1 in carcinogen-induced tongue lesions from *Nsd1* wildtype (WT) mice (top) and *Nsd1* knockout (KO) mice (bottom). Scale bar, 50 μm.

F, Western blots showing STAT1 expression and phosphorylation in *NSD1* wildtype (WT) or knockout (KO) Cal27 cells, or Cal27 cells transfected with *IFNLR1* siRNA.

G, qRT-PCR analysis of representative ISGs in Cal27 cells transfected with control or *IFNLR1* siRNA. Data represent mean ± SD, n=3.

H, Representative immunofluorescent staining of KRT5 and IFNLR1 in *Nsd1* wildtype (WT), *Nsd1* knockout (KO) or *Ifnlr1* knockout (KO) MOC1 cells. Scale bar, 50 μm.

I, Representative immunofluorescent staining of KRT5 and CD8+ T cells in *Ifnlr1* wildtype (WT) or knockout (KO) MOC1 tumors. Bar graph shows the average % immune infiltration into the Krt5+ tumor compartment from at least three regions of interest (ROI) per mouse. Data represent mean ± SD, n=5. Scale bar, 50 μm.

*, $p<0.05$; **, $p<0.01$, ***, $p<0.001$, ****, $p<0.0001$.

See also Figure S5 and Table S2 and S3.

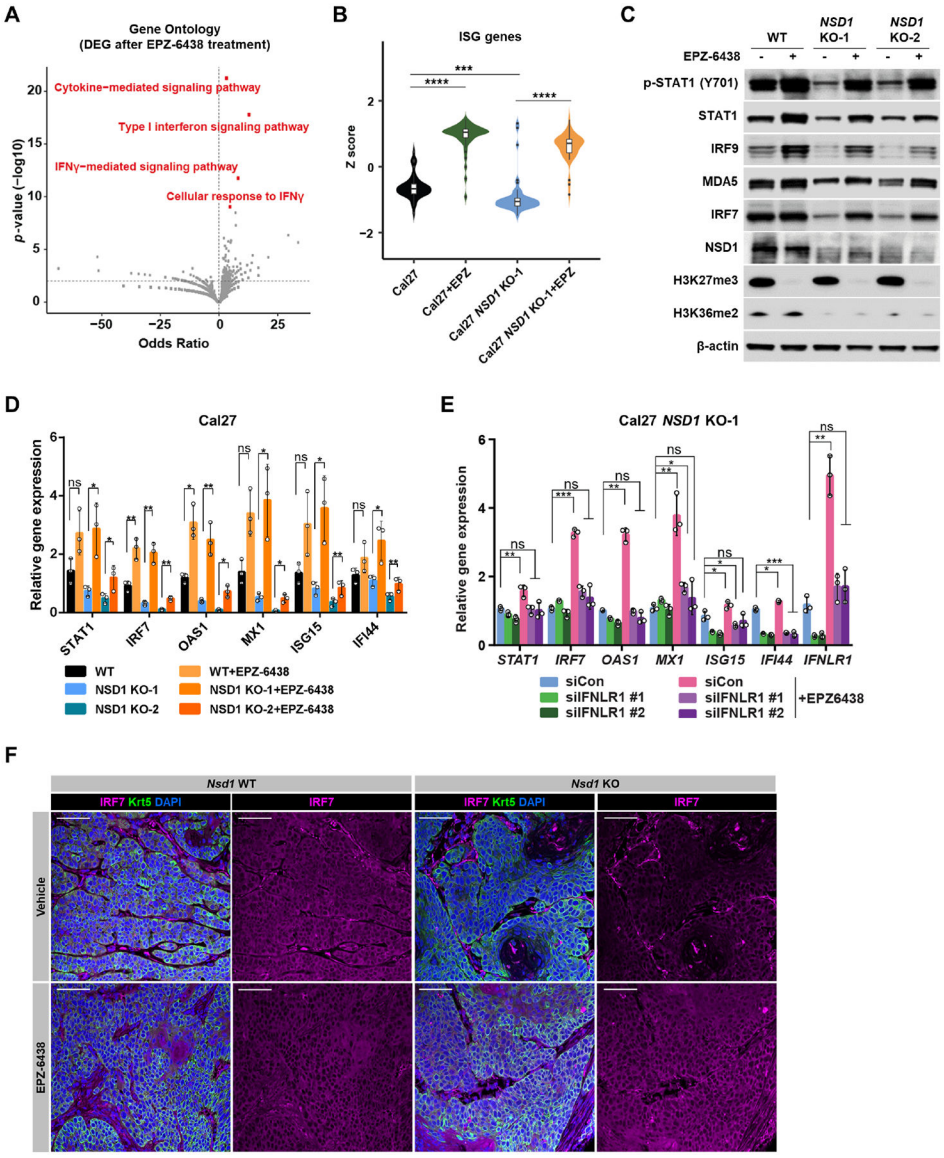

Figure 6: Pharmacologic inhibition of EZH2 but not DNMT1 restores interferon response in NSD1-deficient cells.

A, Gene ontology (GO) analysis of differentially expressed genes between DMSO and EPZ-6438-treated (3 μM for 10 days) *NSD1* knockout (KO) Cal27 cells. The top statistically significantly enriched GO groups among upregulated genes after EPZ-6438 treatment are highlighted in red.

B, Violin plots showing the normalized ISG expression (Z score) of *NSD1* wildtype (WT) and knockout (KO) Cal27 cells with or without the treatment of 3 μM EPZ-6438 for 10 days. The center line in the embedded boxplots represents the median, the box limits are the 25th and 75th percentiles, and the whiskers are the minimum to maximum values. P-values were determined by two-tailed Student's t-test.

C, Western blots showing expression of interferon pathway proteins in *NSD1* wildtype (WT) and knockout (KO) Cal27 cells with or without the treatment of 3 μM EPZ-6438 for 10 days.

D, qRT-PCR analysis of representative ISGs in *NSD1* wildtype (WT) or knockout (KO) Cal27 cells with or without the treatment of 3 μM EPZ-6438 for 10 days. Data represent mean ± SD, n=3.

E, qRT-PCR analysis of *STAT1* and representative ISGs in *NSD1* knockout (KO) Cal27 cells transfected with control or *IFNLR1* siRNA and with or without treatment of EPZ-6438. Data represent mean ± SD, n=3.

F, Representative immunofluorescent staining of KRT5 and IRF7 in *Nsd1* wildtype (WT), left, or *Nsd1* knockout (KO), right, MOC1 tumors with or without EPZ-6438 treatment. Scale bar, 50 μm.

*, $p<0.05$; **, $p<0.01$, ***, $p<0.001$, ns, not significant.

See also Figure S6.

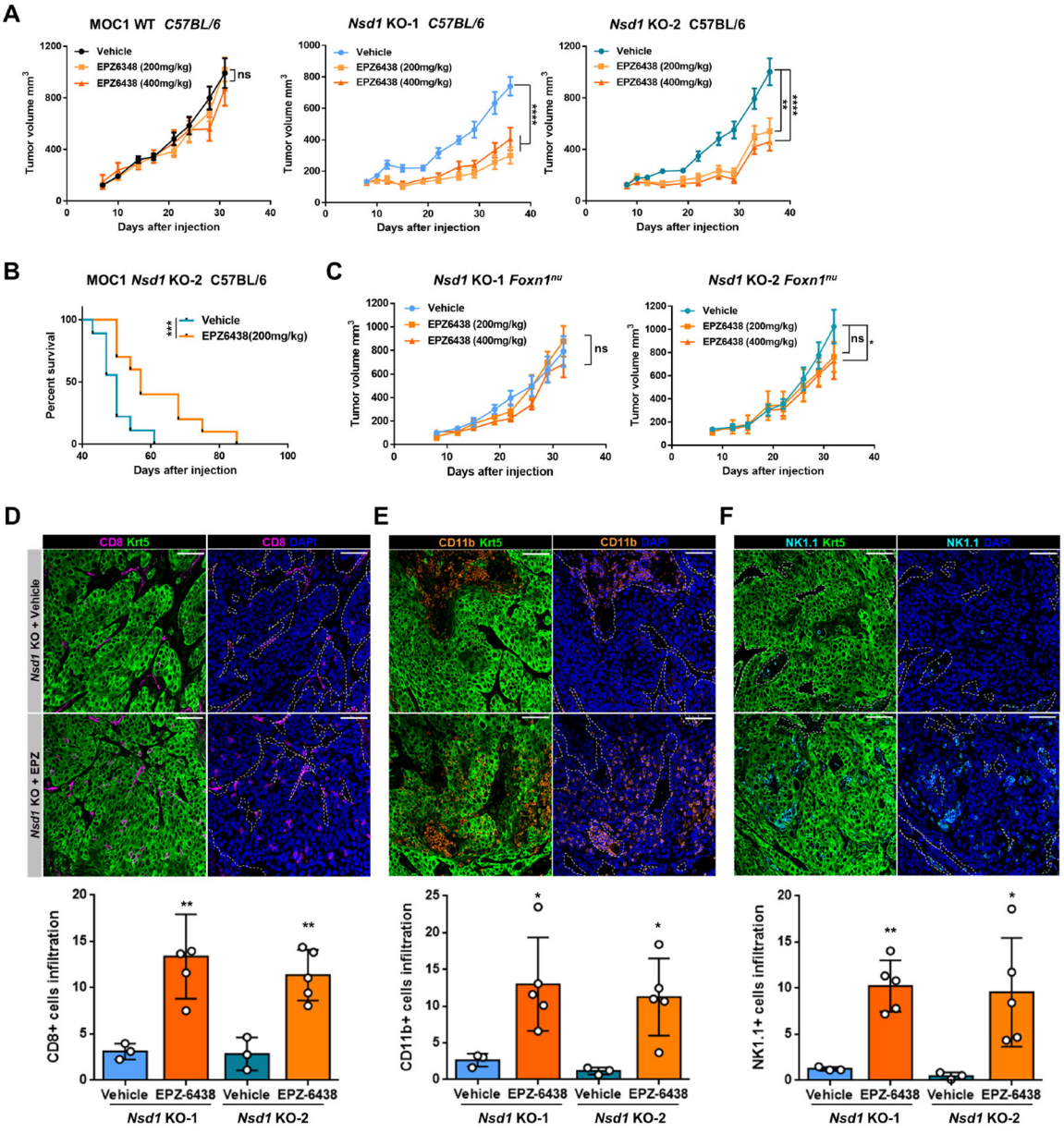

Figure 7: EZH2 inhibitor elicits immune infiltration and inhibits the growth of NSD1-deficient SCC tumors.

A, Volumes of *Nsd1* wildtype (WT) or knockout (KO) MOC1 tumors in C57BL/6 mice treated with vehicle or EPZ-6438 at indicated dosage. Data represent mean ± SEM. n=6–8 per group.

B, Percentage survival of C57BL/6 mice engrafted with *Nsd1* knockout (KO) MOC1 cells treated with vehicle or 200 mg/kg EPZ-6438. Log-rank (Mantel-Cox) test was used to determine significance, n=9–10 per group.

C, Volumes of *Nsd1* knockout (KO) MOC1 tumors in *Foxn1*^{nu} immunodeficient mice treated with vehicle or EPZ-6438 at indicated dosage. Data represent mean ± SEM. n=6–8 per group.

D-F, Representative immunofluorescent staining of Krt5 and CD8+ T cells (D), CD11b+ macrophages (E) and NK1.1+ natural killer (NK) cells (F) in *Nsd1* knockout (KO) MOC1 tumors treated with vehicle or EPZ-6438. Bar graphs below show the average % immune infiltration into the Krt5+ tumor compartment from at least three regions of interest (ROI) per mouse, quantified for each immune cell type (3–7 mice per group; two-sided Student's test; data are represented as mean ± SD). Scale bar, 50 μm.
*, $p<0.05$; **, $p<0.01$, ***, $p<0.001$, ****, $p<0.0001$, ns, not significant.
See also Figure S7.

Key resource Table

REAGENT or RESOURCE	SOURCE	IDENTIFIER
Antibodies		
Alexa Fluor® 700 anti-mouse CD45	Biolegend	Cat#103127
Alexa Fluor® 488 anti-mouse CD90.2	Biolegend	Cat#105315
PE/Cyanine7 anti-mouse CD8a	Biolegend	Cat#100721
Brilliant Violet 605™ anti-mouse NK-1.1	Biolegend	Cat#108739
Brilliant Violet 711™ anti-mouse/human CD11b	Biolegend	Cat#101241
APC anti-mouse CD4	Biolegend	Cat#100515
Rabbit anti-human IFN-lambda R1	Novus	Cat#69635
Mouse anti-human TLR4	R&D systems	Cat#MAB14782
Rabbit anti-human cGAS (D1D3G)	Cell Signaling Technology	Cat#15102S
Mouse anti-human STING/TMEM173	R&D systems	Cat#MAB7169
Mouse anti-IRF-3 (SL-12)	Santa Cruz Biotechnology	Cat#sc-33641
Rabbit anti-IRF3 (phosphor-S386)	Abcam	Cat#ab76493
Mouse anti-TBK1 (108A429)	Santa Cruz Biotechnology	Cat#sc-52957
Rabbit anti-phospho-TBK1/NAK (Ser172) (D52C2)	Cell Signaling Technology	Cat#5483
Rabbit anti-human/mouse Di-Methyl-Histone H3 (Lys36) (C75H12) H3K36me2	Cell Signaling Technology	Cat#2901
Mouse anti-human NSD1	NeuroMab	Cat#Clone N312/10
Rabbit anti-beta Actin	Abcam	Cat#ab8227
Mouse monoclonal anti-dsRNA J2	SCICONS	Cat#10010500
Alexa 488 FITC	ThermoFisher™	Cat#A-11001
Rabbit anti-phospho-Stat1 (Tyr701) (58D6)	Cell Signaling Technology	Cat#9167
Mouse anti-human STAT1	ThermoFisher™	Cat#AHO0832
Mouse anti-mouse Stat1	Santa Cruz Biotechnology	Cat#sc-464
Rabbit anti-IRF7	Cell Signaling Technology	Cat#4920
Rabbit anti-MDA5	Cell Signaling Technology	Cat#5321
Rabbit anti-IRF9	Proteintech	Cat#14167-1-AP
Rabbit anti- Tri-Methyl-Histone H3 (Lys27) (C36B11) H3K27me3	Cell Signaling Technology	Cat#9733
Mouse anti-H3K36me2	Active Motif	Cat#61019
Normal Rabbit IgG	Cell Signaling Technology	Cat#2729
Guinea Pig anti-Rabbit IgG (Heavy & Light Chain)	Antibodies Online	Cat#ABIN101961
Donkey anti-Mouse IgG (H+L)	Sigma-Aldrich	Cat#SAB3701101
Chicken anti-Krt5	Biolegend	Cat#905901
Rabbit anti-NSD1	Bioss	Cat#bs-8170R
Rabbit anti-CD8	Abcam	Cat#ab217344
Rabbit anti-CD11b	Novus Biologicals	Cat#NB110-89474
Mouse anti-NK1.1	Novus Biologicals	Cat#NB100-77528
Rabbit anti-MX1	ThermoFisher™	Cat#13750-1-AP

REAGENT or RESOURCE	SOURCE	IDENTIFIER
Rabbit anti-RSAD2	ProteinTech	Cat#28089-1-AP
Rabbit anti-IRF7	Novus Biologicals	Cat#NBP2-67634
Rabbit anti-IFNLR1	MyBioSource	Cat#MDS7045831
Rabbit anti-Ki67	Abcam	Cat#ab15580
Rabbit anti-Krt13	Lifespan Biosciences	Cat# LS-C22630-1
Mouse anti-Krt10	Novus Biologicals	Cat#NBP2-47825F
Goat anti-P63	R&D Systems	Cat# AF1916
Bacterial and virus strains		
DH5α Competent Cells	Thermo Scientific™	Cat#EC0112
Biological samples		
Human HNSCC patient samples	Laurie Ailles Laboratory	N/A
Chemicals, peptides, and recombinant proteins		
Recombinant Interferon-λ	R&D systems	Cat#1598-IL-025
Tamoxifen	Sigma-Aldrich	Cat#T5648
4NQO	Sigma-Aldrich	Cat#N8141
Hydrocortisone	Sigma-Aldrich	Cat#H0135
Insulin	Sigma-Aldrich	Cat#I6634
Epidermal Growth Factor (EGF)	Sigma-Aldrich	Cat#01-107
Spermidine	Sigma-Aldrich	Cat#S2626
Protease inhibitor cocktail	Sigma-Aldrich	Cat#4693132001
Digitonin	Sigma-Aldrich	Cat#D5628
LPS	Sigma-Aldrich	Cat#L7895
htDNA	Sigma-Aldrich	Cat#D6898
Collagenase IV	ThermoFisher™	Cat#17104019
Dnase I	Sigma-Aldrich	Cat#4716728001
EPZ6438 (Tazemetostat)	MedChemExpress	Cat#HY-13803
5-azacytidine	MedChemExpress	Cat#HY-10586
SGI-110	MedChemExpress	Cat#HY-13542
Critical commercial assays		
Fixable Viability Dye eFluor™ 780	ThermoFisher™	Cat#65-0865
RBC lysis buffer (10X)	Biolegend	Cat#420301
SDS Lysis Buffer	ThermoFisher™	Cat#LC2676
Concanavalin A-coated magnetic beads	Bangs Laboratories	Cat#BP531
NEBNext® High-Fidelity 2X PCR Master Mix	New England Biolabs	Cat#M0541
Ampure XP beads	Beckman Coulter	Cat#A63881
Dynabeads protein A Immunoprecipitation Kit	Invitrogen	Cat#10006D
NucBlue™ Fixed Cell ReadyProbes™ Reagent (DAPI)	Invitrogen	Cat#R37606
TRIzol™ Reagent	Invitrogen	Cat#15596-018
PowerUp™ SYBR™ Green Master Mix	ThermoFisher™	Cat#A25741

REAGENT or RESOURCE	SOURCE	IDENTIFIER
Lipofectamine LTX	ThermoFisher™	Cat#A12621
Lipofectamine RNAiMAX	ThermoFisher™	Cat#13778-150
PCR purification kit	QIAGEN	Cat#28104
PEG-it Virus Precipitation Solution	SystemBio	Cat#LV810A-1
Mut Express II Fast Mutagenesis Kit V2	Vazyme	Cat#C214-01
2'3'-cGAMP ELISA kit	Cayman	Cat#501700
IFN-λ2/λ3 ELISA kit	R&D systems	Cat#DY1789B
M-PER™ Mammalian Protein Extraction Reagent	ThermoFisher™	Cat#78503
Deposited data		
Cut & Tag sequencing data	This paper/GEO	GSE186239
RNA-seq data	This paper/GEO	GSE186239
Cancer genomic data	TCGA/cBioportal	N/A
Cancer dependency data	Depmap	N/A
Tumor immune estimation data	TIMER	N/A
Experimental models: Cell lines		
Human: Cal27	ATCC	Cat#CRL-2095™
Human: FaDu	ATCC	Cat#HTB-43™
Human: Detroit 562	ATCC	Cat#CCL-138™
Human: BICR78	Sigma-Aldrich	Cat#04072111
Human: SKN-3	JCRB cell bank	Cat#JCRB1039
Human: PE/CA-PJ15	Sigma-Aldrich	Cat# 96121230
Human: SK-MES-1	ATCC	Cat#HTB-58™
Mouse: MOC1	Kerafast	Cat#EWL001-FP
Mouse: MOC1 Nsd1 KO#1	This paper	N/A
Mouse: MOC1 Nsd1 KO#2	This paper	N/A
Mouse: MOC1 Ifnlr1 KO	This paper	N/A
Human: Cal27 NSD1 KO#1	This paper	N/A
Human: Cal27 NSD1 KO#2	This paper	N/A
Human: SK-MES-1 NSD1 KO	This paper	N/A
Human: Detroit 562 NSD1 KO	Farhangdoost et al., 2021	N/A
Human: FaDu NSD1 KO	Farhangdoost et al., 2021	N/A
Experimental models: Organisms/strains		
Mouse: C57BL/6J	The Jackson Laboratory	Cat#000664 RRID:IMSR_JAX:000664
Mouse: Foxn1^{nu}	Charles River	Cat#007850 RRID:IMSR_JAX:007850
Mouse: NOD.Cg-Prkdcscidll2rgtm1Wjl/SzJ (NSG)	The Jackson Laboratory	Cat# 005557 RRID:IMSR_JAX:005557
Mouse: Nsd1$^{f/f}$	This paper	N/A

REAGENT or RESOURCE	SOURCE	IDENTIFIER
Mouse: Krt5^{CreERT2}	D. Metzger and P. Chambon	N/A
Oligonucleotides		
Cloning primers	This paper	Supplemental Table S4
ChIP primers	This paper	Supplemental Table S4
Real-time PCR primers	This paper	Supplemental Table S4
Recombinant DNA		
pCDH-EF1-MCS-IRES-Puro	System Biosciences	Cat#CD532A-2
pSpCas9(BB)-2A-GFP (PX458)	Addgene	Cat#48138
pCDH-EF1-MCS-IRES-Puro-NSD1 truncation	This paper	N/A
pCDH-EF1-MCS-IRES-Puro-NSD1R2017Q truncation	This paper	N/A
pU6-pegRNA-GG-acceptor	Addgene	Cat#132777
pUiSEPR	Dr. Scott Lowe	N/A
pCMV-PE2	Addgene	Cat#132775
pL-CRISPR.EFS.tRFP	Addgene	Cat#57819
pVSV-G	Addgene	Cat#138479
psPAX2	Addgene	Cat#12260
dCas9VPR-Neo	Addgene	Cat#63798
Software and algorithms		
ImageJ software (v1.8.0)	National Institutes of Health	https://imagej.nih.gov/ij/
GraphPad Prism (v6.0)	GraphPad software lnc	https://www.graphpad.com
Qupath	Bankhead et al., 2017	https://qupath.github.io/
FlowJo™ (V10)	FlowJo, LLC	https://www.flowjo.com/
BioRender	BioRender	https://biorender.com/
Benchling	Benchling	https://www.benchling.com/crispr